ADVANCED FUNCTIONAL MATERIALS

Supporting Information

for *Adv. Funct. Mater.,* DOI: 10.1002/adfm.202108047

Highly Transparent and Conductive Indium-Free Vanadates Crystallized at Reduced Temperature on Glass Using a 2D Transparent Nanosheet Seed Layer

*Alexis Boileau, Simon Hurand, Florent Baudouin, Ulrike Lüders, Marie Dallocchio, Bruno Bérini, Aimane Cheikh, Adrian David, Fabien Paumier, Thierry Girardeau, Philippe Marie, Christophe Labbé, Julien Cardin, Damien Aureau, Mathieu Frégnaux, Maryline Guilloux-Viry, Wilfrid Prellier, Yves Dumont, Valérie Demange, and Arnaud Fouchet**

Supporting Information of:

Highly transparent and conductive indium-free vanadates crystallized at reduced temperature on glass using a 2D transparent nanosheet seed layer

Alexis Boileau[1], Simon Hurand[2], Florent Baudouin[3], Ulrike Lüders[1], Marie Dallocchio[1], Bruno Bérini[4], Aimane Cheikh[1], Adrian David[1], Fabien Paumier[2], Thierry Girardeau[2], Philippe Marie[5], Christophe Labbé[5], Julien Cardin[5], Damien Aureau[6], Mathieu Frégnaux[6], Maryline Guilloux-Viry[3], Wilfrid Prellier[1], Yves Dumont[4], Valérie Demange[3], Arnaud Fouchet[1]*

1 NORMANDIE UNIV, ENSICAEN, UNICAEN, CNRS, CRISMAT, 14000 CAEN, France

2 Institut Pprime, UPR 3346 CNRS-Université de Poitiers-ENSMA, SP2MI, 86962 Futuroscope-Chasseneuil Cedex, France

3 Univ Rennes, CNRS, ISCR – UMR 6226, ScanMAT – UMS 2001, F-35000 Rennes, France

4 GEMaC, CNRS UMR 8635, Université de Versailles Saint-Quentin-en-Yvelines – Université Paris-Saclay, 45 Av. des États-Unis, 78035 Versailles, France

5 CIMAP, NORMANDIE UNIV, ENSICAEN, UNICAEN, CEA, CNRS, 14000 Caen, France

6 ILV, CNRS UMR 8180, Université de Versailles Saint-Quentin-en-Yvelines – Université Paris-Saclay, 78035 Versailles, France

* Corresponding author:

E-mail: arnaud.fouchet@ensicaen.fr

Keywords: transparent conducting oxide (TCO), $CaVO_3$ (CVO) and $SrVO_3$ (SVO) perovskite thin films, correlated metals, nanosheets, spectroscopic ellipsometry

1. Deposition of $SrVO_3$ thin films on glass without CNO NS seed layer

Two $SrVO_3$ (SVO) thin films have been deposited on 5 × 5 mm^2 Eagle XG Corning® glass substrate at 400 °C and 700 °C by pulsed laser deposition (PLD). The growth conditions are similar to those of films deposited on $Ca_2Nb_3O_{10}^-$ nanosheets (CNO NS) seed layer on

glass substrate. A KrF excimer laser (λ = 248 nm) was used with a repetition rate of 3 Hz and a laser fluence adjusted at 1.6 J.cm^{-2} to get a deposition rate close to 0.1 Å per laser pulse. The films thickness was increased to 100 nm by adjusting the number of pulse to unambiguously detect the amorphous character of the films. As expected, SVO films deposited on glass are entirely XRD-amorphous between 400 and 700 °C (figure S1).

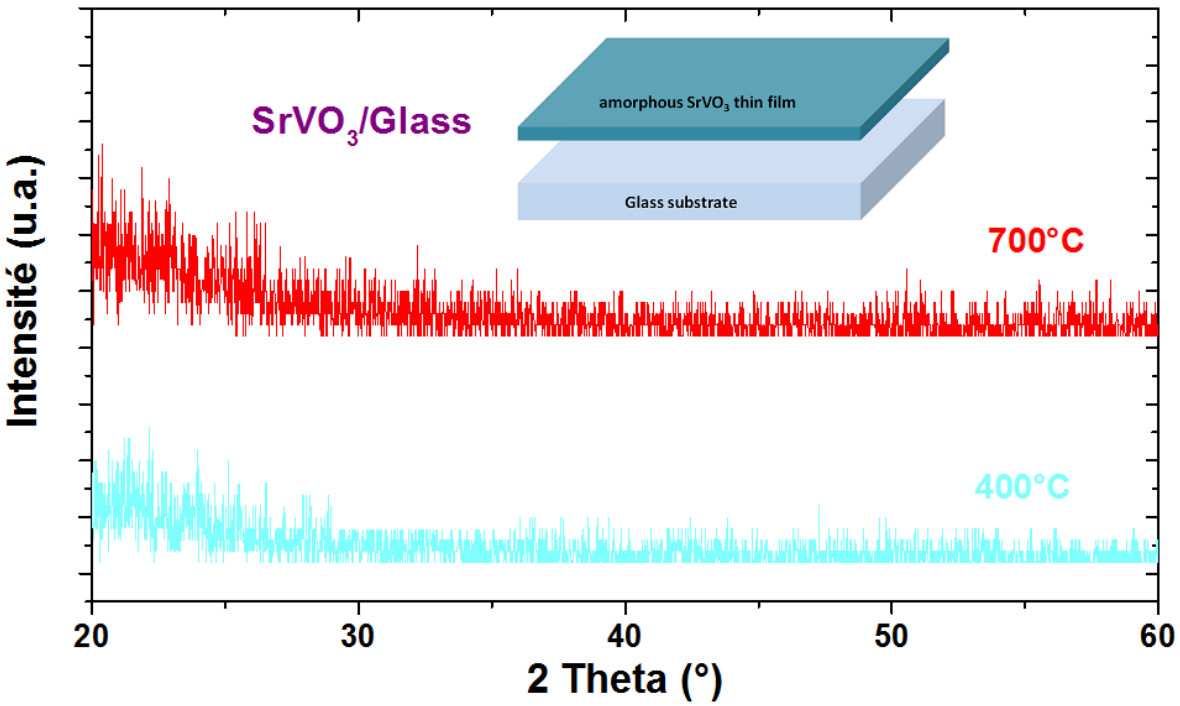

Figure S1. X-ray diffraction patterns of 100 nm thick SVO thin films deposited on Eagle XG Corning® glass substrate at 400 °C and 700 °C by PLD.

2. Structural, chemical and morphological characterizations

2.1. Investigation of the morphology of the NS seed layer by atomic force microscopy

A pristine sample of $Ca_2Nb_3O_{10}^-$ nanosheets deposited on Eagle XG Corning® glass substrate is imaged by atomic force microscopy (AFM) in tapping mode using a Pico SPM-LE microscope of Molecular Imaging. Acquired images are processed with the Gwyddion free software. The AFM image displayed in figure S2 (a), shows the NS dispersed over the glass surface. The NS are juxtaposed alongside each other even if NS overlap in some places. The size of the NS is between 100 nm to 2 μm for the largest ones. In order to extract more information about the NS stacking due to the multi-steps approach of the Langmuir-Blodgett (LB) process, the AFM image is processed by selective height thresholding of the glass surface and the NS layers (figure S2 (b)). In this way, we are able to retrieve three NS layers (L1, L2 and L3). Then, the statistical analysis of each mask gives its average height ($z_{average}$) and its percentage of coverage (P_x).

First, we can calculate the "local" coverage P_L of the glass surface with the entire NS seed layer as follows:

$$P_L = 100 - P_{GS} = 90.74\ \% \qquad \text{(A)}$$

Thus, the "local" coverage is close to 90 % indicating a dense coverage of the glass surface.

Secondly, we can calculate the relative thickness of each layer (t_x) by subtracting to $z_{average}$ the height of each preceding layers. Values are reported in figure S2 (c) for reworked images. Finally, the average thickness t_{NS} of the entire NS seed layer which is weighted by the percentage of coverage of each layer can be easily determined as follows:

$$t_{NS} = t_{L1} \times (P_{L1} + P_{L2} + P_{L3}) + t_{L2} \times (P_{L2} + P_{L3}) + t_{L3} \times (P_{L3}) \qquad \text{(B)}$$

The average thickness of the entire NS seed layer t_{NS} is found to be 2.93 nm.

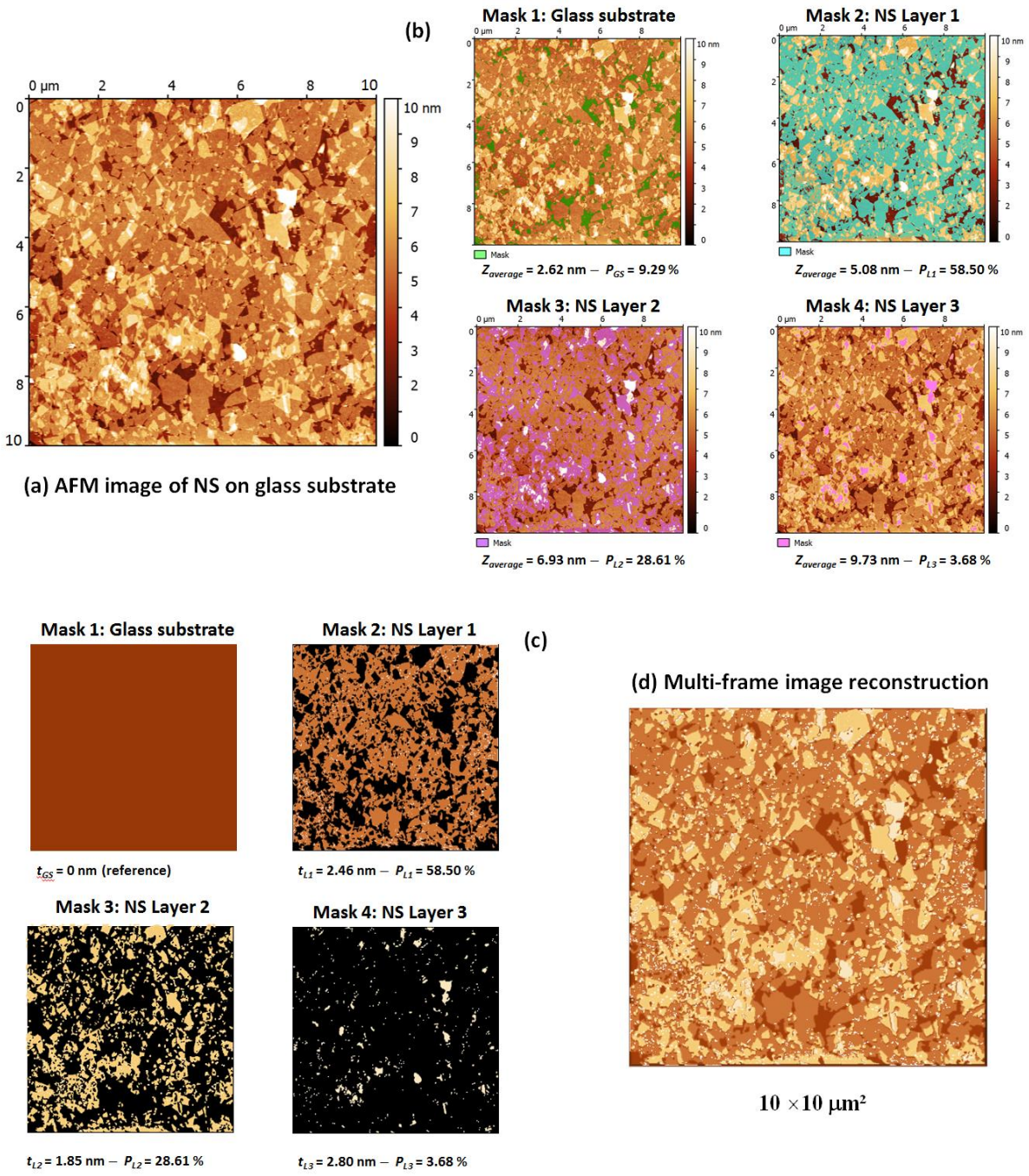

Figure S2. (a) AFM image of a pristine sample of CNO NS deposited on glass. (b) Creation of masks by selective height thresholding of the different layers (glass surface and NS layers). The average height ($z_{average}$) of each mask and its percentage of coverage (P_x) are extracted. (c) Data processing of selected masks. The relative thickness (t_x) of each layer is reported here. (d) Multi-frame image reconstruction from masks in (c) confirming identical image to the starting AFM image. All images measure 10 ×10 μm^2.

2.2. Determination of the film thickness

The thickness determination of deposited vanadates thin films was realized by X-ray reflectometry (XRR) measurements, performed on a Bruker D8 Discover diffractometer operating with monochromatic Cu $K_{\alpha 1}$ radiation (λ = 1.5406 Å). Note that only oscillations ascribed to the vanadate layer are discernible. Both CNO NS seed layer and amorphous $LaAlO_3$ layer are too thin to produce observable oscillations. The measured thicknesses are in good agreement with the targeted thickness (40 nm).

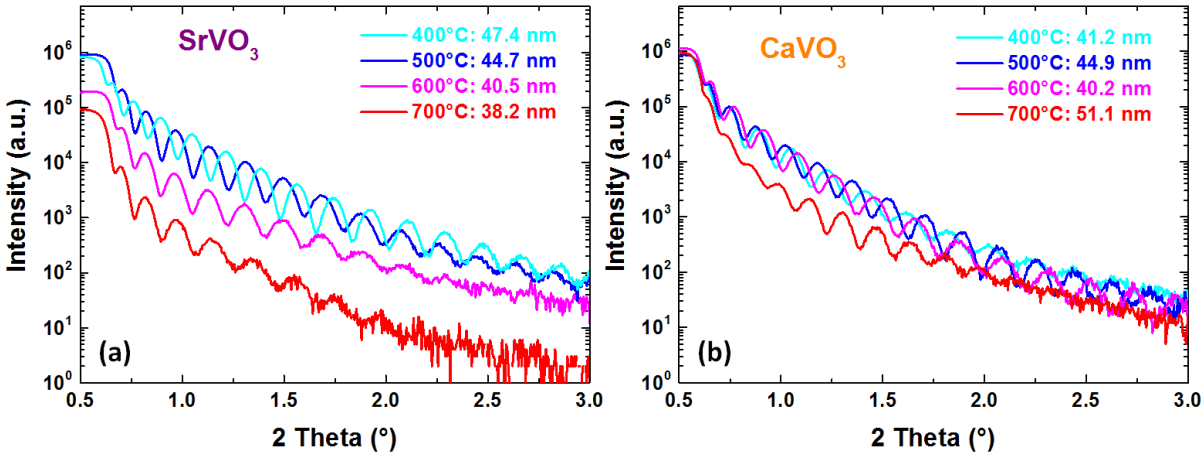

Figure S3. XRR of SVO (a) and CVO (b) thin films deposited at different growth temperatures onto CNO NS prepared glass substrate used to determine the film thickness.

2.3. Investigation of the morphology of vanadate films

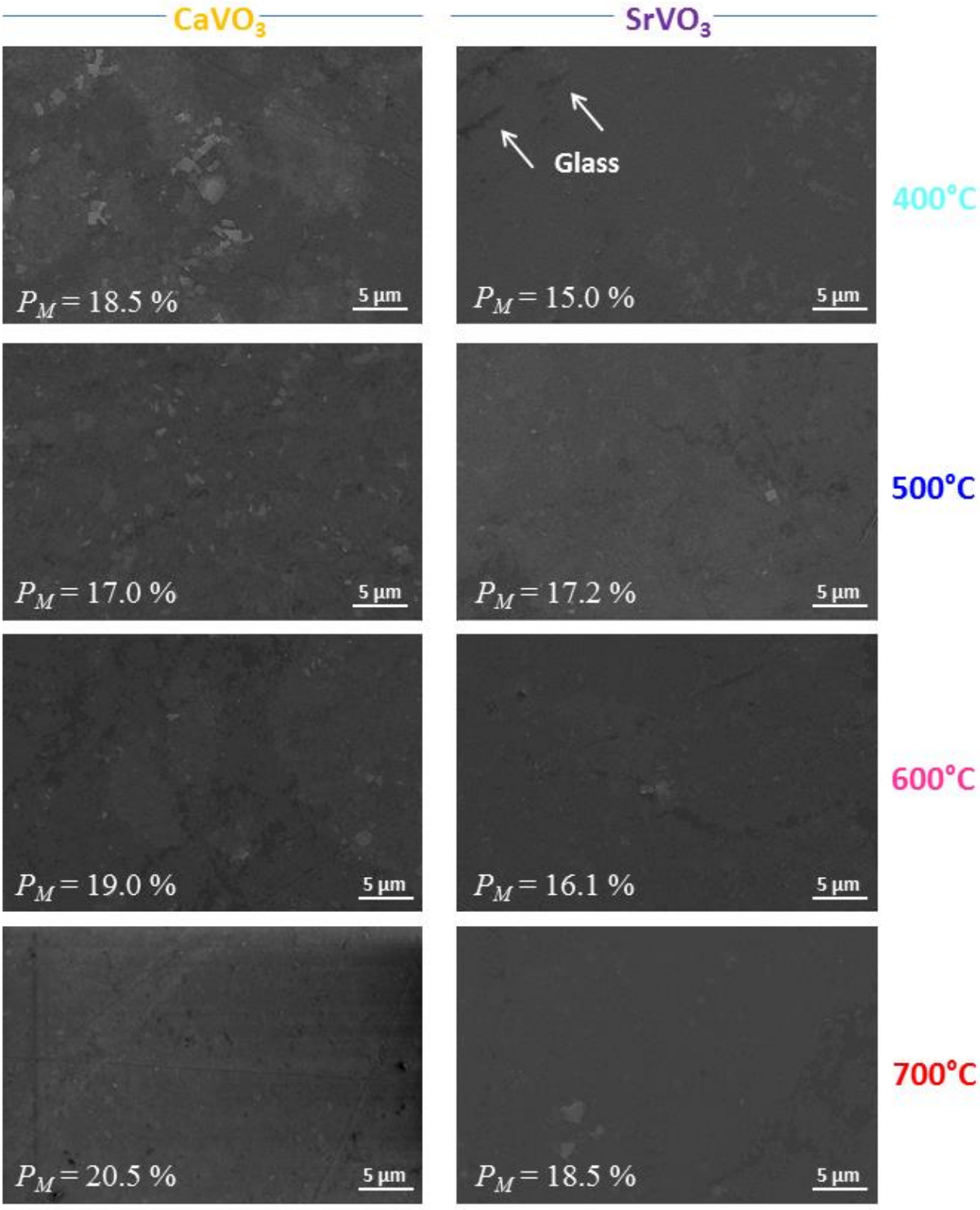

Figure S4. Scanning electron microscopy micrographs of CNO NS coated on glass substrates used for different growth temperatures of CVO and SVO films. The percentage of macroscopic coverage (P_M) averaged from different images is reported here for information. The darker areas correspond to the uncovered glass substrate.

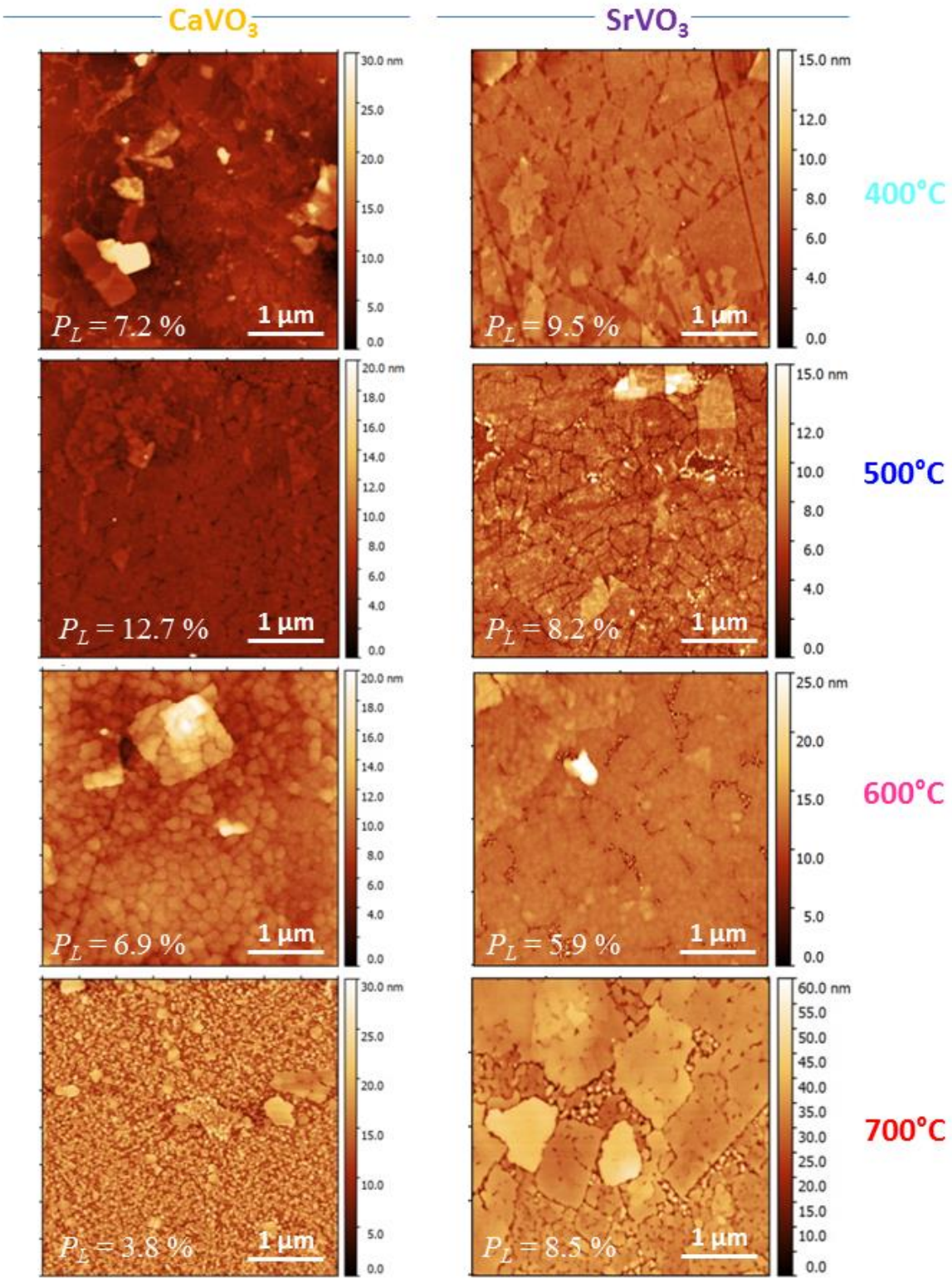

Figure S5. 4 × 4 µm² AFM images of CVO and SVO films deposited at different temperatures. The percentage of local coverage (P_L) averaged from different images is reported here for information.

From the AFM images displayed in figure S5, the morphology of CVO and SVO films seem to be dependent on the growth temperature (T_G) by the establishment of a granular microstructure at higher T_G. This evolution is confirmed by the root mean square (RMS) roughness increasing between 400 to 700 °C from 0.27 (0.13) nm up to 1.09 (1.24) nm for CVO (SVO) surfaces. An increase of the grain size with T_G has been already observed for $La_{0.67}Sr_{0.33}MnO_3$ films grew on NS deposited on glass.[1] High temperature activates the diffusion of species over the surface during the growth, which leads to a morphological modification of films. Nevertheless, structural change of the NS with T_G and the Eagle XG Corning® glass transformation near the softening point at 669 °C cannot be totally excluded and complementary analysis should be done which are out of scope of this publication.

The percentage of global surface coverage ($P_{coverage}$) of glass substrates by the NS seed layer can be easily extracted from the microscopy micrographs. This parameter is determined by taking into account the percentage of macroscopically uncovered areas (p_M) observed in the SEM images (figure S4) and the percentage of local uncovered areas (p_L) too small to be observed by SEM and determined by AFM (figure S5). These values are reported for all samples in table S1 with an average of p_M ~19 % and p_L ~ 8 %, respectively. $P_{coverage}$ is then determined by the combination of p_M and p_L as $(1-p_M)\times(1-p_L)$ leading to a typical value of ~ 74 % (values are reported in table S1 and figure 1 (f) in the main text).

2.4. Investigation of the chemical composition and the structure of vanadate films by transmission electron microscopy

2.4.1. Films composition

According to the deposition temperatures, diffusion of glass elements into the films may be the cause of the increase of the lattice parameters together with the decrease of the X-ray diffraction intensity. Substrate and films compositions (figures S6.a,b,c) were measured by energy dispersive X-ray spectroscopy (EDXS) coupled to a transmission electron microscope (TEM). The Eagle XG Corning® glass is mainly made of Si, O, Al and Ca, together with few amount of Mg (see figure S6.a). Spectrum of the CVO and SVO grown at 500 °C shows only elements of the film (i.e. CVO and SVO coated by LAO), together with X-ray line of the TEM copper microgrid (see figure S6.b,c). For CVO, a usual very small Si Kα peak in the

EDX spectrum can also be seen; it results from the Si crystal of the detector. Interestingly, spectra of CVO films grown at higher temperatures show a higher Si Kα peak revealing the diffusion of this element from the glass into the films. Concerning the SVO films, the energy of the principal Lα1,2 emission line of strontium (E = 1.81 keV) falls at the same position than the Si Kα1,2 lines (1.74 keV) (figure S6.c); therefore, the diffusion of the Si in SVO films is not observable by this method. Whereas for both vanadates, the small lines of Nb L are discernible, coming from diffusion of Nb from the nanosheets into the films. Nb is only observed at high temperature for both films as already observed for the silicon. It has to be noted that diffusion of substrate elements in the film was already observed in one of our previous study also at high temperature[2].

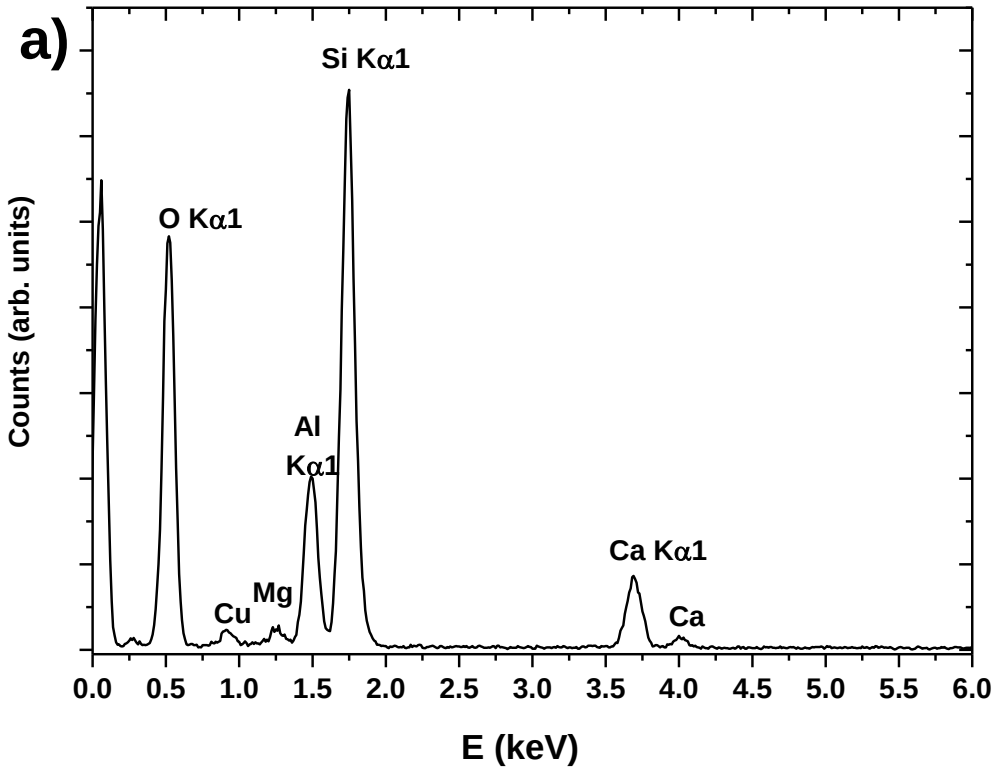

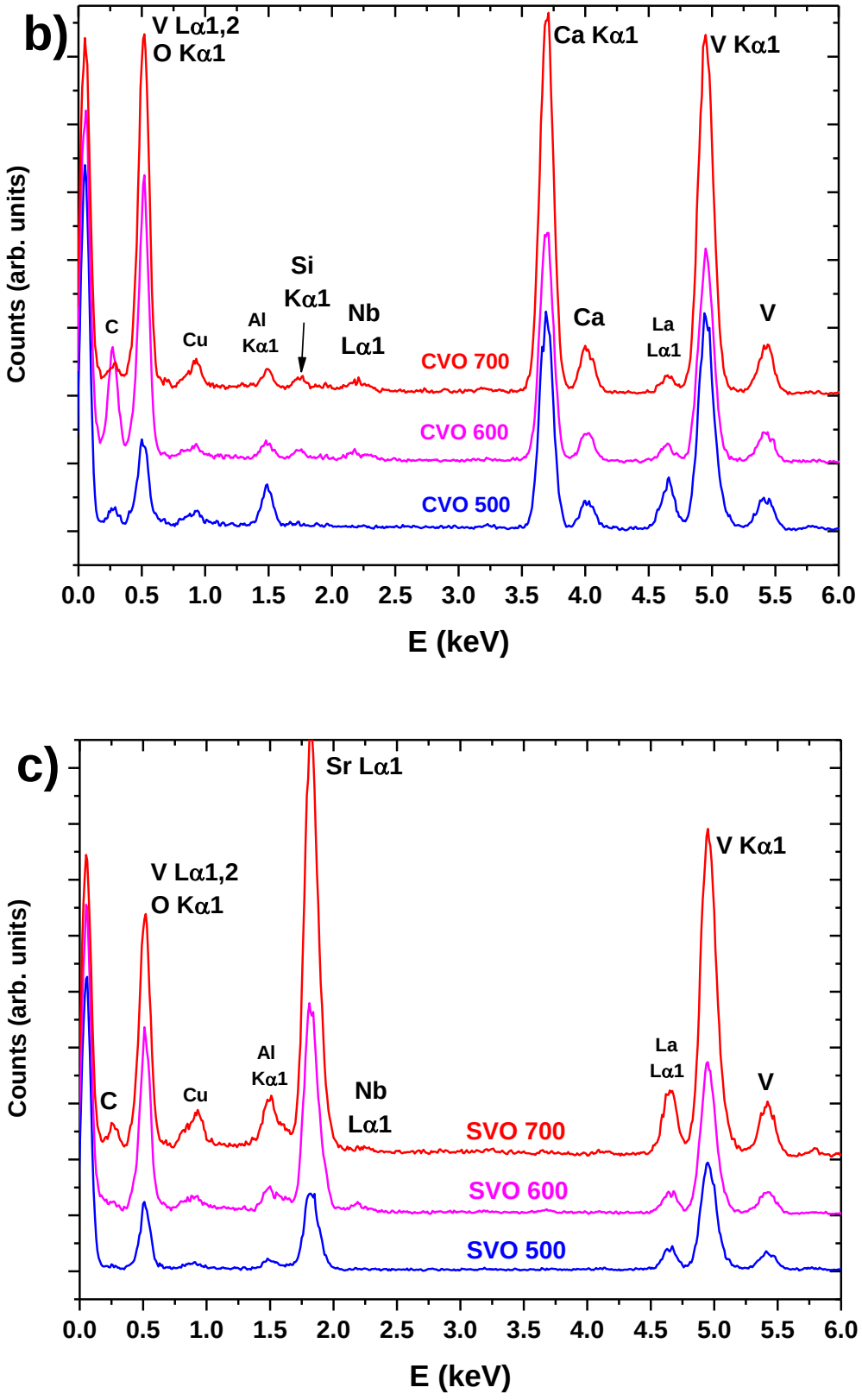

Figure S6. a) EDX spectrum of the Eagle XG Corning® glass. b) EDX spectra of the CVO films. c) EDX spectra of the SVO films.

2.4.2. Structural analysis of vanadate films

(a) TEM results

TEM analyses were performed on CVO and SVO grown at 500 °C. Bright field in-plane view micrographies show that the films are dense and made of grains that are connected by grain boundaries (figure S7a,b for CVO and S8a,b,c for SVO). These grain boundaries are very fine as shown in figures S7c,d and no pores between grains are observed. Electron diffraction patterns of a fragment of SVO film grown at 500 °C were recorded for two different grains. These patterns show the same [001] zone axis for both grains, but with an in-plane rotation relatively to each other. These results confirm the preferential [001] orientation of the film grown on nanosheets template, with an in-plane texturation.

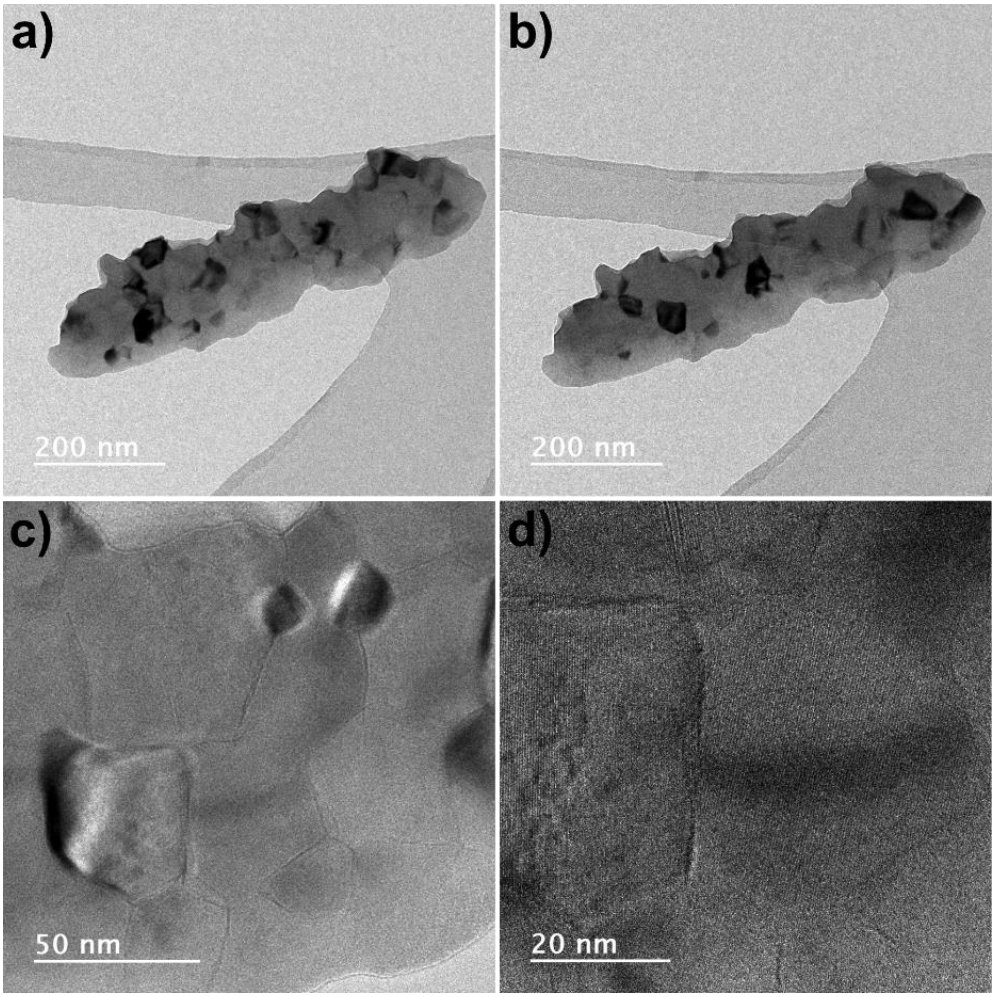

Figure S7. a,b) Bright field TEM micrographies of a fragment of CVO film grown at 500 °C along two different orientations showing the grains forming the film. c) Bright field TEM micrography at higher magnification under overfocus condition allowing a high contrast of grains boundaries. d) High magnification micrography of an area showing grains and grain boundaries.

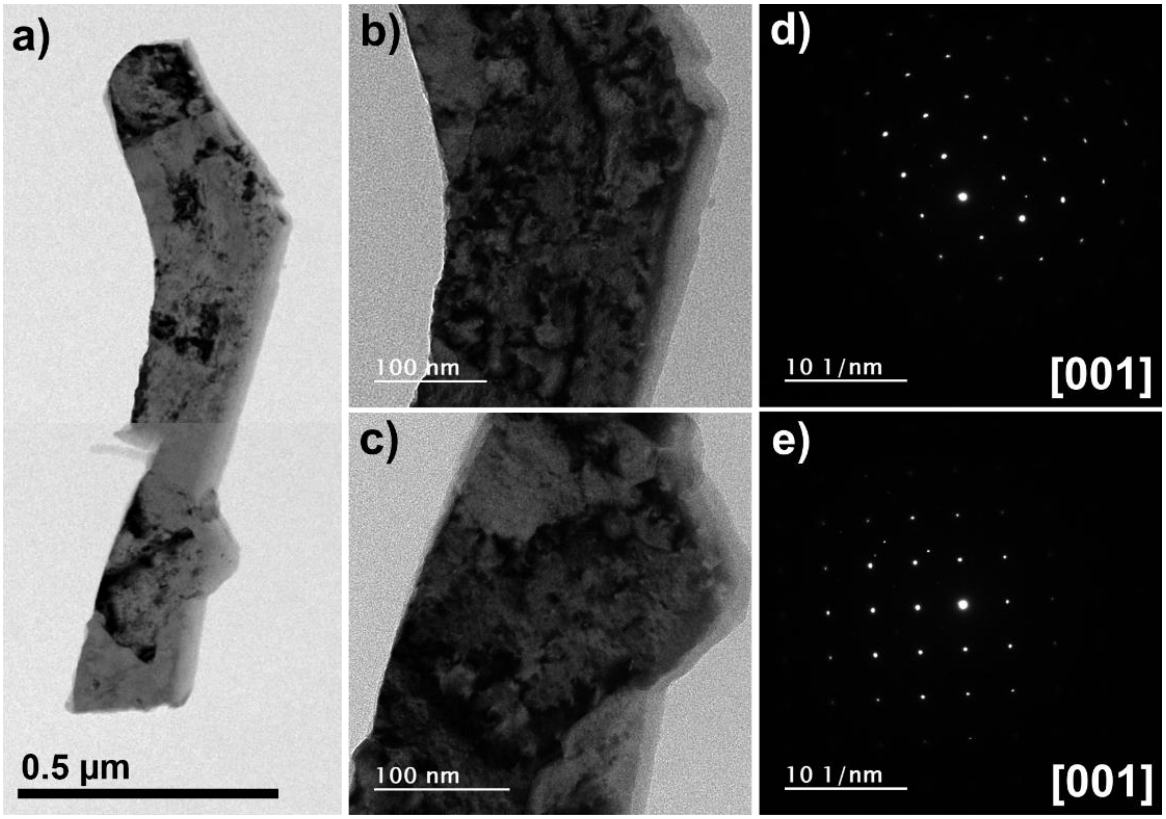

Figure S8. a) Bright field TEM micrography of a fragment of SVO film grown at 500 °C. b,c) Bright field TEM micrographies at higher magnification showing grains and grain boundaries of two different areas of the film. d,e) Corresponding zone axis patterns along the [001] zone axis.

(b) In-plane XRD

In-plane XRD was performed on CVO and SVO films grown at 500, 600 and 700 °C. Full-range diagrams show the peaks of vertical crystallographic planes (figure S9a,b). Diagrams recorded around the 004 (CVO) and 200 (SVO) reflexions reveal that the peak positions are shifted to high angles with the increase of the growth temperature (figure S9c,d) for both vanadates. The evolutions of the in-plane lattice parameter deduced from these patterns are displayed figure S10. For SVO film the in-plane parameter is practically equal to its out-of-plane counterpart (cf. table S1) which is showing that the films are relaxed. At the contrary for CVO, the films undergo a tensile strain induced by the nanosheets. The evolution as a function of the growth temperature is identical for both vanadates. The unit cell volume is decreasing from 55.037 $Å^3$ to 54.638 $Å^3$ for CVO and from 58.945 $Å^3$ to 58.099 $Å^3$ for SVO.

These evolutions can be related to the insertion of Si and Nb in the film as shown by EDX measurements together with presence of oxygen vacancies.

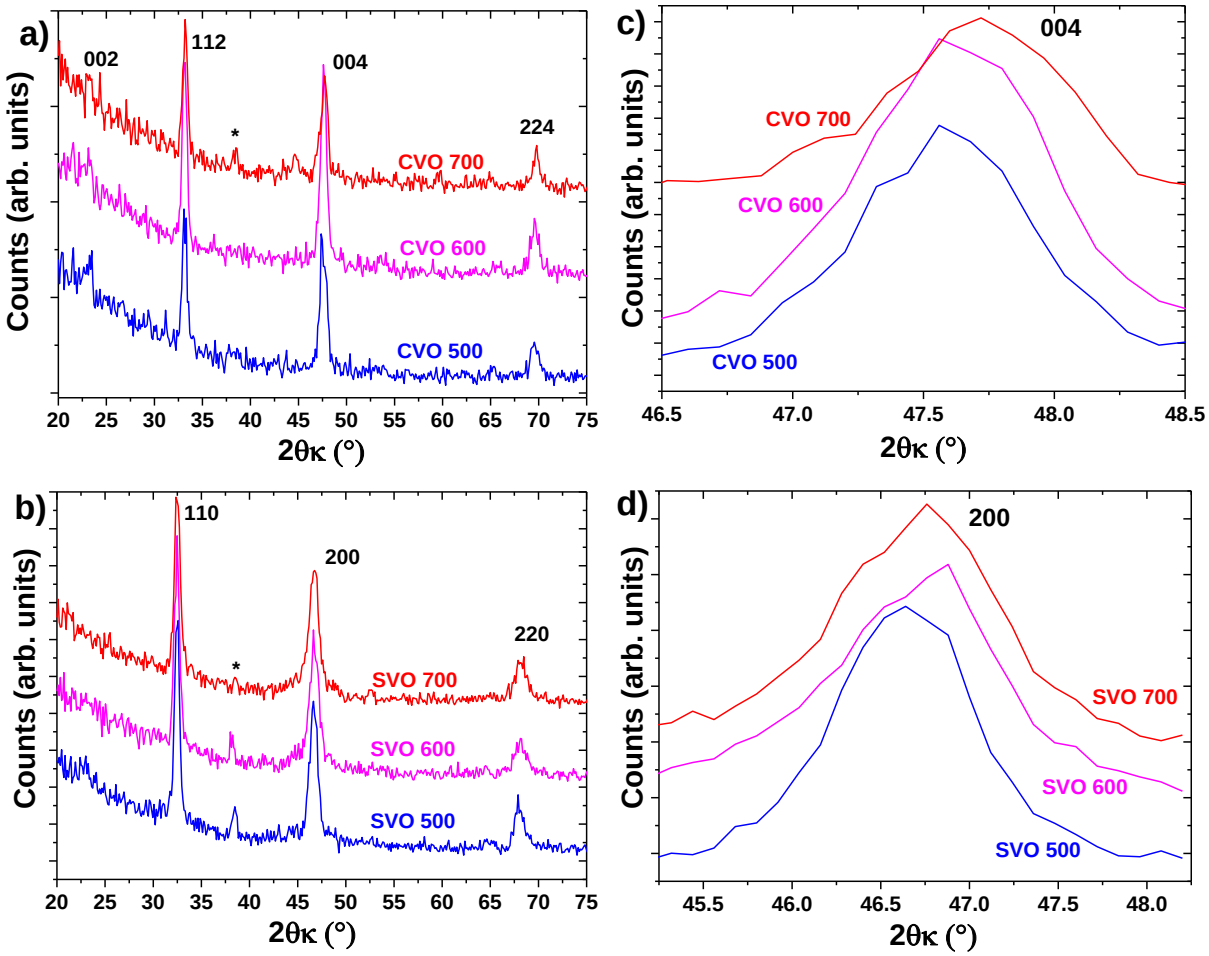

Figure S9. In-plane X-ray diffraction diagrams of CVO films (a) full-range; c) around the 004 reflexion) and SVO films (b) full-range; d) around the 200 reflexion) (*: holder).

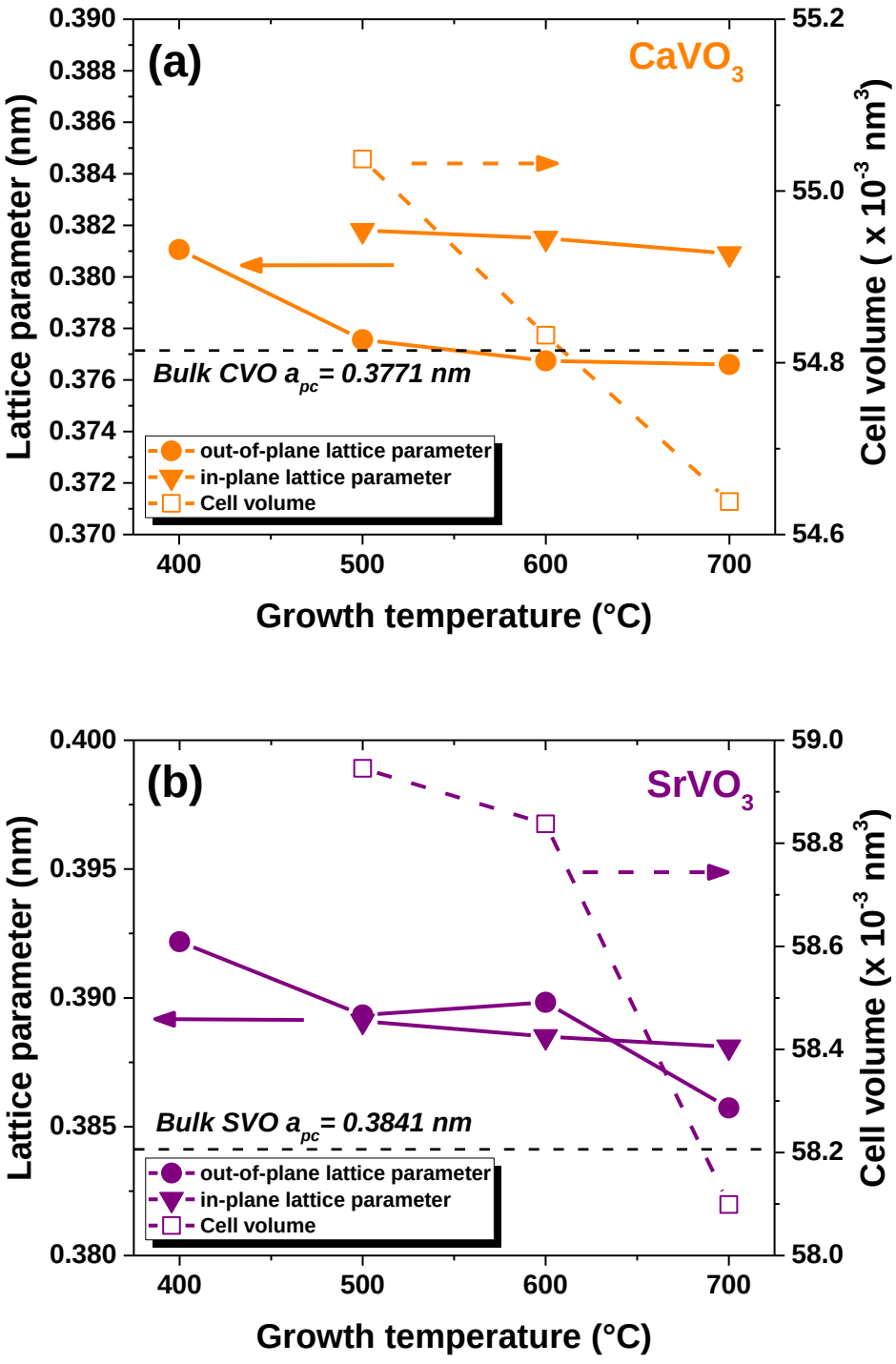

Figure S10. Evolution of the in-plane (measured by in-plane XRD) and out-of-plane lattice parameters (measured by θ-2θ X-ray diffraction) and the cell volume as a function of the growth temperature of CVO (a) and SVO (b) thin films.

2.5. Investigation of the depth chemical profiling vanadate films by X-ray photoelectron spectroscopy

X-ray photoelectron spectroscopy (XPS) depth profiling is the best tool to evidence the cationic out-diffusion from the substrate with the growth temperature. Indeed, in the case of XPS analysis, the detection threshold is close to 0.1 % atomic whereas this limit is higher for EDX analysis (in general, higher than 0.2 % atomic). In this goal, CVO films deposited at 500 and 700°C have been chemically characterized by XPS time–resolved analysis under argon etching beam. The experimental procedure is described in details in the main text of the article (see experimental section). The figures S11 (a) and (b) show the evolution of the atomic percentage of cations as function of the etching time for films deposited at 500 and 700°C, respectively. The comparison of depth profiles for Si 2s peak (figure S12) between 500 and 700°C shows a more pronounced profile at high temperature with Si upcoming in higher content and earlier than Si 2s profile of film deposited at 500°C. Similar evolution is also observed for Nb 3d depth profiles (figure S13) confirming the diffusion of Nb into the CVO layer. In conclusions, the XPS depth profiling confirms that Si diffuses from the glass substrate and Nb from the CNO nanosheet seed layer into the CVO layer faster at 700°C than 500°C.

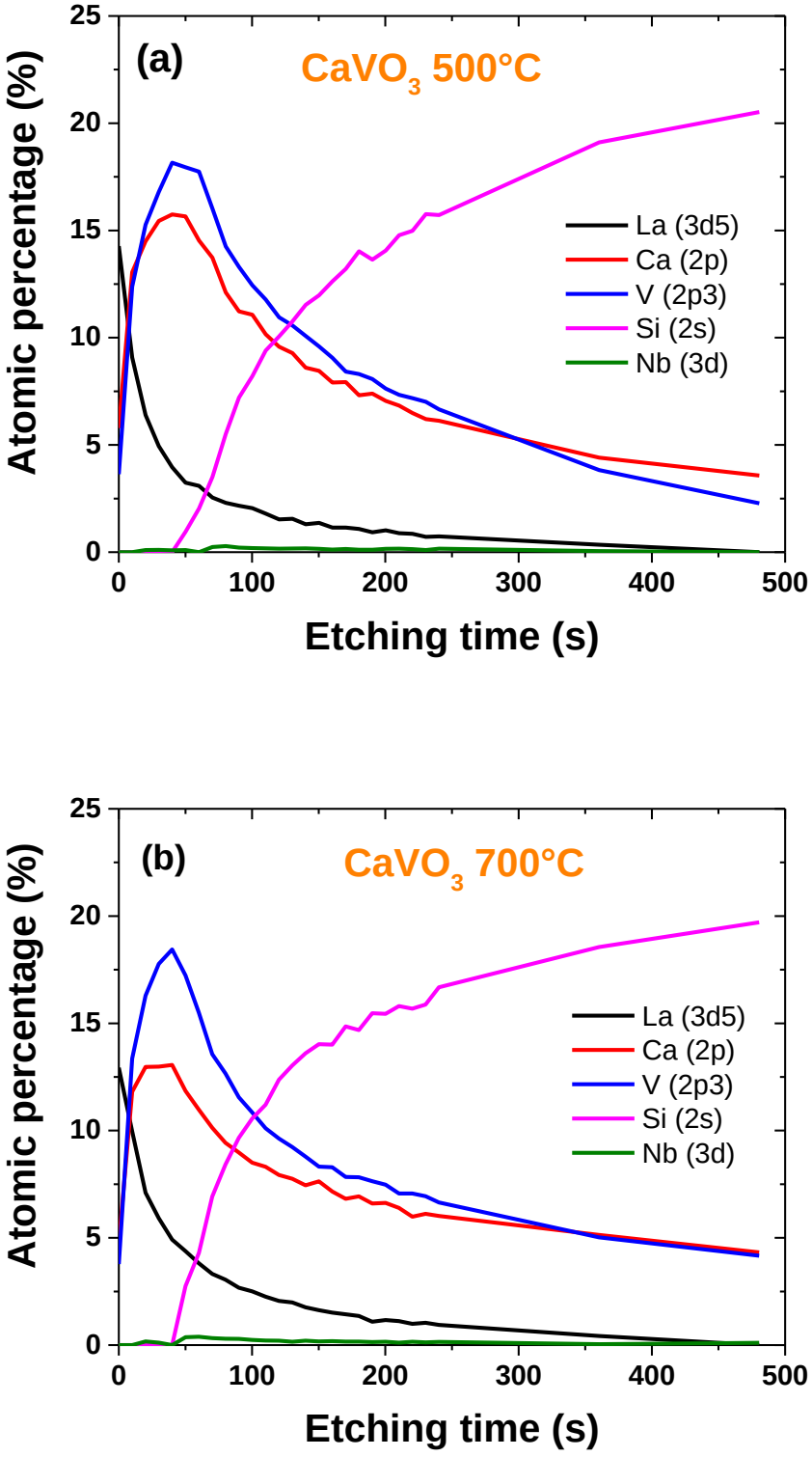

Figure S11. Time resolved XPS depth profiles of cations for CVO films deposited at 500°C (a) and 700°C (b).

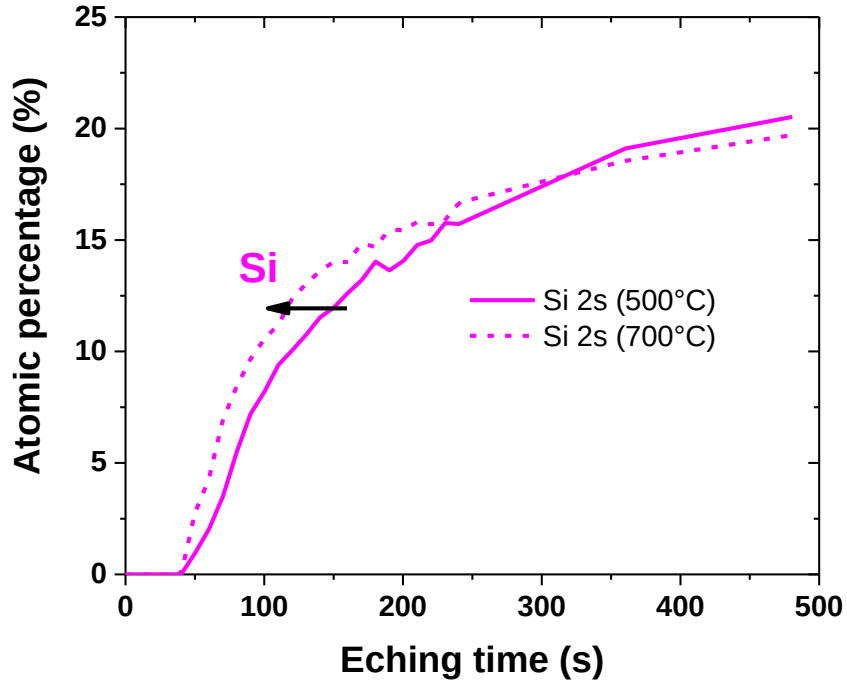

Figure S12. Comparison of Si2s XPS depth profiles of CVO films grown at 500°C (solid line) and 700°C (dash line).

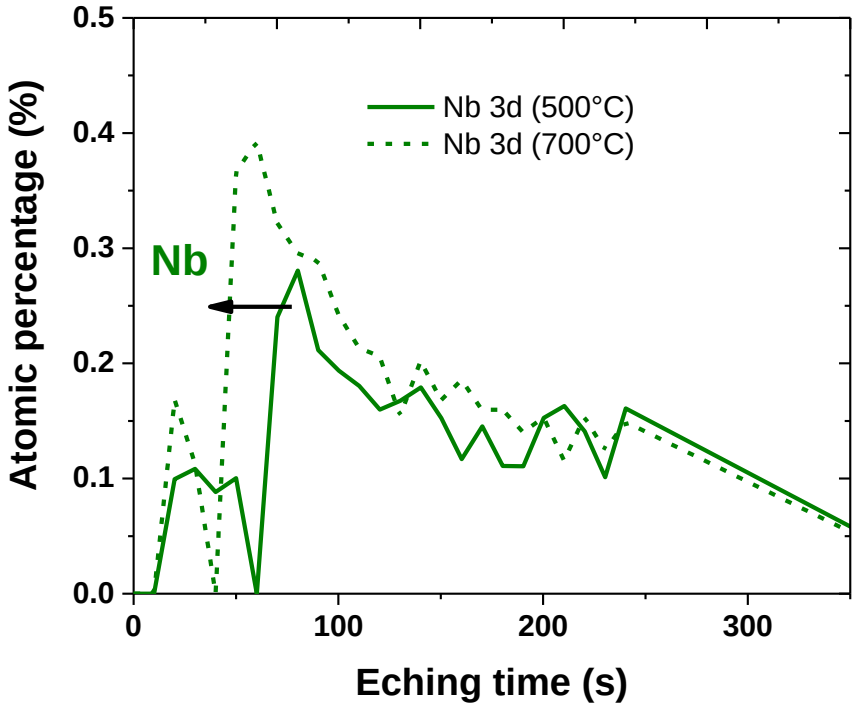

Figure S13. Comparison of Nb3d XPS depth profiles of CVO films grown at 500°C (solid line) and 700°C (dash line).

Table S1. Summarized data of the microstructural investigations of CVO and SVO films on CNO NS/GS

Sample	T_G [°C]	Thickness [nm]	p_M [%]	p_L [%]	$P_{coverage}$ [%]	$P_{amorphous}$ [%]	$P_{crystalliezd}$ [%]	P_{EBSD} [%]	*RMS Roughness* [nm]	*Ou lattic*
CVO	400	41,2	18.5	7.2	75.6	-	-	-	0.27	
CVO	500	44.9	17.0	12.7	72.4	30.2	69.8	65.0	0.51	
CVO	600	40.2	19.0	6.9	75.4	32.0	68.0	-	0.74	
CVO	700	51.1	20.5	3.8	76.5	27.7	72.3	-	1.09	
SVO	400	47.4	15.0	9.5	76.9	-	-	-	0.13	
SVO	500	44.7	17.2	8.2	76.0	27.2	72.8	75.3	0.52	
SVO	600	40.5	16.1	5.9	79.0	19.9	80.1	-	0.43	
SVO	700	38.2	18.5	8.5	74.6	31.5	68.5	-	1.24	

Legend: growth temperature (T_G), percentage of macroscopic uncovered glass zones determined by SEM (p_M), percentage of local uncovered glass zones determined by AFM (p_L), percentage of total coverage of glass by NS ($P_{coverage}$) extracted from microscopy analysis, percentage of amorphous phase determined by ellipsometry ($P_{amorphous}$), percentage of crystallized phase determined by SE ($P_{crystallized}$), percentage of crystallized phase determined by EBSD (P_{EBSD}), root-mean-square roughness of films (*RMS roughness*), out-of-plane lattice parameter determined by θ-2θ XRD, in-plane lattice parameter determined by in-plane XRD and cell volume.

3. DC Transport properties

The DC resistivity measurement have been performed using the four-probe method with the Van der Paw configuration from 5 to 370 K in a physical properties measurement system (PPMS) designed by Quantum Design.

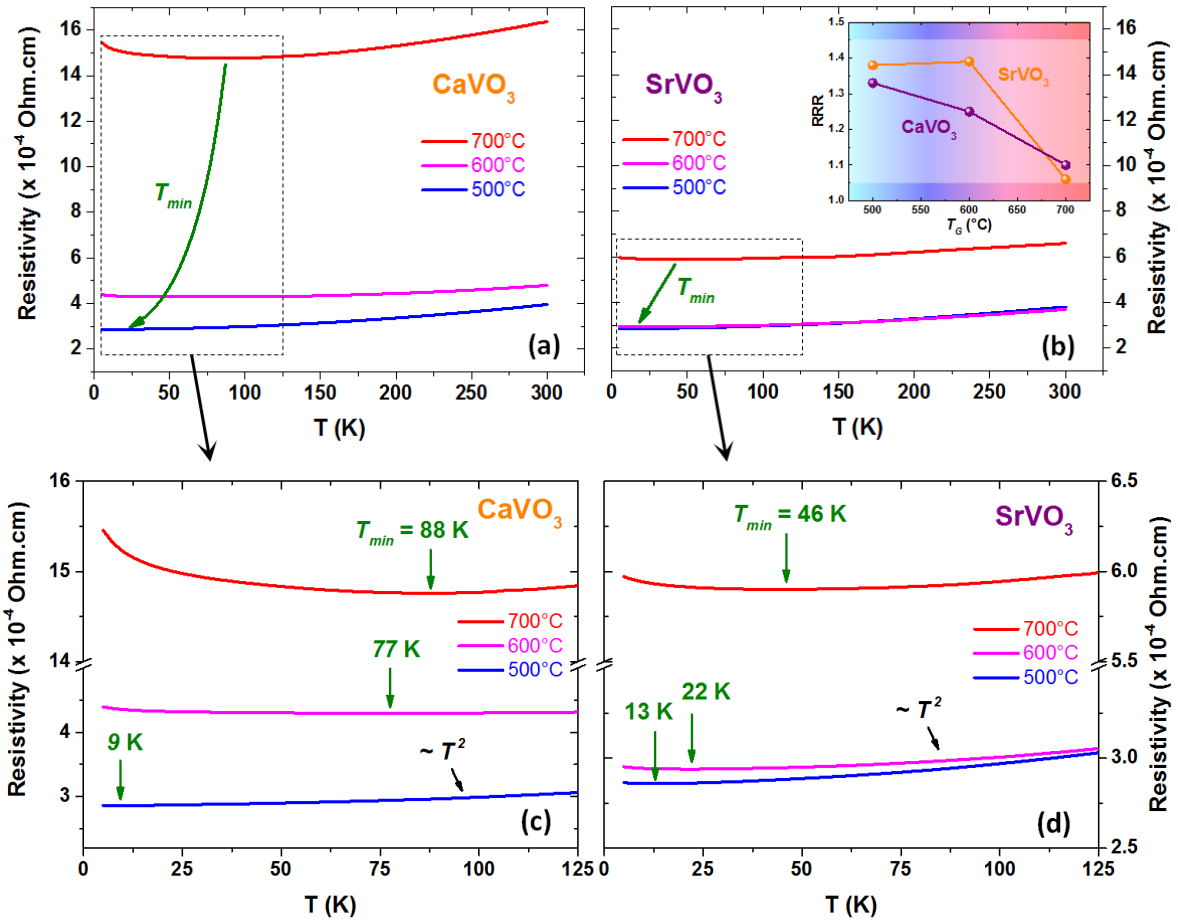

Figure S14. Temperature-dependent resistivity curves of CVO (a) and SVO (b) deposited on CNO NS/GS. The insert in (b) shows the residual resistivity ratio (*RRR*) of films as function of the growth temperature. Figures (c) and (d) focus on the resistivity upturn below T_{min} defined as the resistivity minimum occurring in the low temperature range.

The temperature dependence of the electrical resistivity is plotted in figure S14 (a) and (b) for textured CVO and SVO thin films grown between 500 °C and 700 °C. Vanadate films deposited at 400 °C are weakly crystallized and therefore too resistive to be measured. For all metallic films, room temperature resistivity (ρ_{300K}) is within restrictive range going from 3.65 $\times$ 10^{-4} Ω.cm to 1.64 $\times$ 10^{-3} Ω.cm. These values are consistent with those reported for bulk vanadates ranging from 7.0 $\times$ 10^{-4} Ω.cm [3,4] to 4.2 $\times$ 10^{-2} Ω.cm [5] and thin films with values between 2.84 $\times$ 10^{-5} Ω.cm [6] and 2.90 $\times$ 10^{-3} Ω.cm [7]. The resistivity is extremely low considering that near 30% of our textured vanadate films is amorphous and the presence of grain boundaries in the structure. Nevertheless, the percolation of well crystallized and highly textured CVO or SVO domains onto CNO NS as revealed by EBSD imaging is sufficient to ensure enough conduction pathways and the delocalization of correlated electrons through the

film. However, in low temperature range, the electrical behavior exhibits a metal-insulator-like transition defined as the resistivity minimum observed at T_{min} (figures S14 (c) and (d)). All values summarized in table S2 show that T_{min} shifts with T_G increasing from 9 to 88 K for CVO films and from 13 to 46 K for SVO films. Fouchet *et al.* have already observed the appearance of a similar metal insulator transition moving from 10 to 85 K when the thickness of single crystal SVO thin films is reduced from 7 to 3 nm.[8] However, authors show that correlations with in-plane and out-of-plane structural stress evolutions show the existence of a 7 nm relaxation thickness corresponding to the metallic state limit. In our case, locally epitaxially grown films are too thick to follow this model. Electronic localization at grain boundaries can be responsible of the upturn of the resistivity in low temperature range. This assertion is reinforced together by AFM imaging where a granular microstructure takes shape with T_G (figure S5). As a result, the metallic state is remarkably stabilized for films deposited at low temperature and the resistivity of textured vanadate films largely did not exceed values typically reported for standard TCOs as ITO [9], demonstrating excellent electrical properties. For this reason, these results are a great improvement for vanadate integration onto thermal sensitive substrates.

For the metallic regime identified above T_{min}, the resistivity follows a quadratic temperature dependence fitted on the basis of the typical model for metallic conductors defined as:

$$\rho(T) = \rho_0 + A \times T^{\alpha} \qquad \text{(C)}$$

where ρ_0 is the residual resistivity at 0 K related to the background contribution due to the static disorder, and $A \times T^{\alpha}$ accounts for electron correlation effects in Fermi liquid description (here, A is related to electron-electron scattering).[10–12] The fit results are summarized in table S2. Values for thin films are consistent with those reported for bulk CVO and SVO materials for which A is ranging from 4.0×10^{-10} [13,14] to 6.0×10^{-8} Ω.cm.K^{-2} [5]. In the Fermi liquid model, the residual resistivity ρ_0 leads to values between 6.0×10^{-6} [12–14] and 3.0×10^{-2} Ω.cm [5]. The values presented in table S1 are showing that the quality of our CVO and SVO films are comparable to single crystals and thin films. Nevertheless, the gradual increase of ρ_0 from 2.86×10^{-4} (2.86×10^{-4}) to 1.46×10^{-2} Ω.cm (5.86×10^{-4} Ω.cm) between 500 and 700 °C for CVO (SVO) indicates that crystalline defects as the out-diffusion of elements from the glass substrate evidenced by coupled TEM-EDXS analysis (figure S6) are promoted by the temperature increasing. Similarly, the residual resistivity ratio (*RRR*) defined as the ratio

ρ_{300K}/ρ_{5K} reported in insert of figure S14 (b), does not exceed 1.38 and decreases slightly with T_G. The ratio RRR < 2 [15] is related to the presence of the crystalline disorder due to the in plane disorientation of the films and the grain boundaries, the presence of cations coming from the substrate by diffusion with the T_G increasing, and probably can also be related to the presence of oxygen vacancies in the structure at higher temperatures.

Table S2. Summarized data of the DC transport properties of CVO and SVO films on CNO NS/GS

Sample	T_G [°C]	ρ_{300K} [Ω.cm]	ρ_{5K} [Ω.cm]	*RRR* [-]	$R_{\square}$ [Ω.sq^{-1}]	T_{min} [K]	ρ_0 [Ω.cm]	$A\times10^{-10}$ [Ω.cm.K^{-2}]	α [-]	$N_{DC}\times$ [cm
CVO	400	-	-	-	-	-	-	-	-	
CVO	500	3.95×10^{-4}	2.86×10^{-4}	1.38	19.44	9	2.86×10^{-4}	18.30	1.93	2.
CVO	600	3.65×10^{-4}	2.63×10^{-4}	1.39	21.58	77	2.60×10^{-4}	9.81	2.03	2.
CVO	700	1.64×10^{-3}	1.55×10^{-3}	1.06	20.03	88	1.46×10^{-3}	2.34	2.37	2.
SVO	400	5.15×10^{-1}	1.58×10^{-2}	-	23992	-	-	-	-	
SVO	500	3.81×10^{-4}	2.86×10^{-4}	1.33	18.79	13	2.86×10^{-4}	12.30	1.98	1.
SVO	600	3.70×10^{-4}	2.95×10^{-4}	1.25	20.14	22	2.93×10^{-4}	4.81	2.10	1.
SVO	700	6.59×10^{-4}	5.97×10^{-4}	1.10	38.09	46	5.86×10^{-4}	6.53	2.05	1.

Legend: Growth temperature (T_G), RT resistivity (ρ_{300K}), resistivity at 5 K (ρ_{5K}), residual resistivity ratio (RRR), sheet resistance ($R_{\square}$), temperature of the resistivity minimum (T_{min}), residual resistivity (ρ_0), temperature prefactor of the Fermi liquid theory (A), temperature exponent (α), DC charge carrier density (N_{DC}), DC charge carrier mobility (μ_{DC}), DC scattering time (τ_{DC}). DC resistivity reduced by the factor f of crystalline phase ($\rho_{DC} \times f$).

4. Spectroscopic ellipsometry study of $CaVO_3$ and $SrVO_3$ thin films

4.1. Spectroscopic ellipsometry

All the films were characterized by Variable Angle Spectroscopic Ellipsometry (VASE) both from ultraviolet to near-infrared range (UV-vis-NIR, from 0.7 eV to 5.9 eV) with a J. A. Woollam M2000XI, and in the infrared range (IR, from 0.04 eV to 0.7 eV) with a J. A. Woollam IR-Vase Mark II. The ellipsometric angles Ψ and Δ are measured at incident angles of 55°, 65° and 75°. The UV-vis-NIR and the IR data are then spliced together and analyzed

concomitantly with the CompleteEase software supported by the J. A. Woolam Company. An optical model is built that includes the different layers, their dielectric functions (DFs) and their thicknesses, using several fitting parameters. Numerical regression using a Levenberg-Marquardt algorithm is performed to adjust the fitting parameters in order to obtain agreement between the Ψ and Δ angles predicted by the model and the ones measured. This is done by minimizing the Mean-Square Error (*MSE*), defined in the CompleteEase software by the formula:

$$MSE_{NCS} = \sqrt{\frac{1}{3n-m}\sum_{i=1}^{n}\left[\left(\frac{N_{E_i}-N_{G_i}}{.001}\right)^2 + \left(\frac{C_{E_i}-C_{G_i}}{.001}\right)^2 + \left(\frac{S_{E_i}-S_{G_i}}{.001}\right)^2\right]} \qquad \text{(D)}$$

Where "n" is the number of wavelengths, "m" is the number of fit parameters, $N = \cos(2\Psi)$, $C = \sin(2\Psi)\cos(\Delta)$, $S = \sin(2\Psi)\sin(\Delta)$.

The samples of interest are composed of a stack of several layers, as shown on figure S15: an Eagle XG glass substrate; a $Ca_2Nb_3O_{10}^-$ nanosheets seed layer (hereafter named NS); a $CaVO_3$ or $SrVO_3$ layer (hereafter named CVO (SVO)); and an amorphous $LaAlO_3$ layer (hereafter named a-LAO). In order to determine the dielectric functions (DFs) of CVO or SVO in our films, it is necessary to determine the thicknesses and DFs of all the other layers separately as a first step. For this purpose, we first study a NS thin film and an aLAO thin film deposited alone on a (111) silicon substrate. The sections below detail the characterization of all substrates and layers.

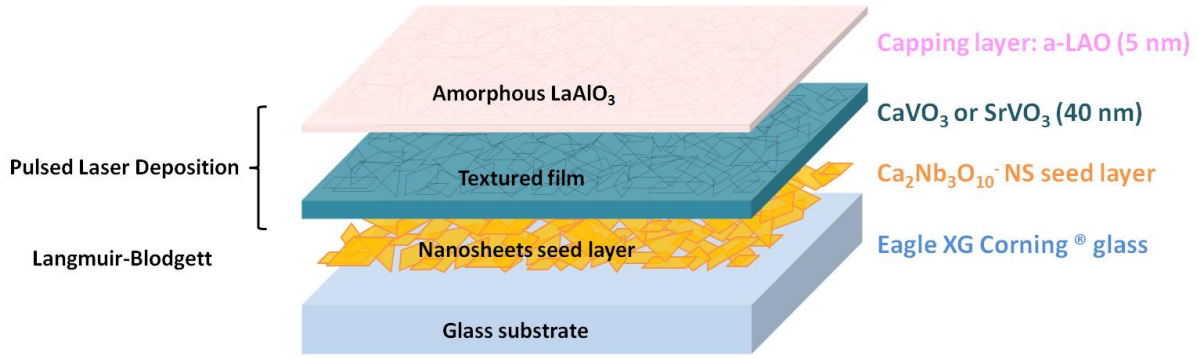

Figure S15. Scheme of the complete sample stacks.

4.2. (111) silicon substrate

The pristine (111) silicon substrate was characterized using a two-layer optical model: (1) a semi-infinite Silicon substrate, which DFs are taken as tabulated values provided from J. A. Woolam (SI_JAW); (2) a thin layer of native silicon oxide, which DFs are also taken as tabulated values provided from J. A. Woolam (NTVE_JAW). The substrate is single-side polished and the backside reflections can be neglected: this is confirmed by the very weak depolarization measured on the whole measurement range (less than 3 % from 0.04 to 5.0 eV). Surface roughness, angle offset and thickness non-uniformity of the film were not taken into account as they have been found to have insignificant influence on the model. The only fit parameter is the thickness of the native oxide layer, which is found equal to 1.60 nm.

4.3. Amorphous $LaAlO_3$

A 5 nm thick amorphous layer of $LaAlO_3$ (a-LAO) was deposited onto a (111) silicon substrate by PLD with the same deposition parameters as the ones used to cover the CVO-SVO layer. The (111) silicon substrate originates from the same wafer as the one characterized in the previous section, so that the DFs and thicknesses of the Silicon and Native Silicon Oxide layers are fixed to the ones previously determined. LAO is an insulator with a wide band gap of 5.6 eV and is transparent in the whole measurement range. A very precise study of the DFs of amorphous LAO can be found e.g. in ref.[16]. The DFs of the a-LAO were modelled by a simple Cauchy dispersion law with no absorption ($k = 0$):

$$n(\lambda) = A + \frac{B}{\lambda^2} + \frac{C}{\lambda^4} \qquad \text{(E)}$$

We further assume $C = 0$, as is often the case for transparent materials. The simplicity of the Cauchy model – with only 2 fitting parameters in this case, A and B – allows simultaneous fitting of the optical constants and the thickness. We found a thickness of 5.39 nm, very close to the nominally deposited thickness of 5 nm. The resulting DFs are very similar to the ones of ref.[16].

- Layer # 2 = LAOa Cauchy Thickness # 2 = **5.39 nm** (fit) A = **1.828** (fit) B = **0.01368** (fit) C = 0.0000 + **Urbach Absorption Parameters**
Layer # 1 = NTVE_JAW Oxide Thickness = 1.60 nm
Substrate = SI_JAW

Figure S16. Optical model for the sample with a-LAO on a (111) silicon substrate.

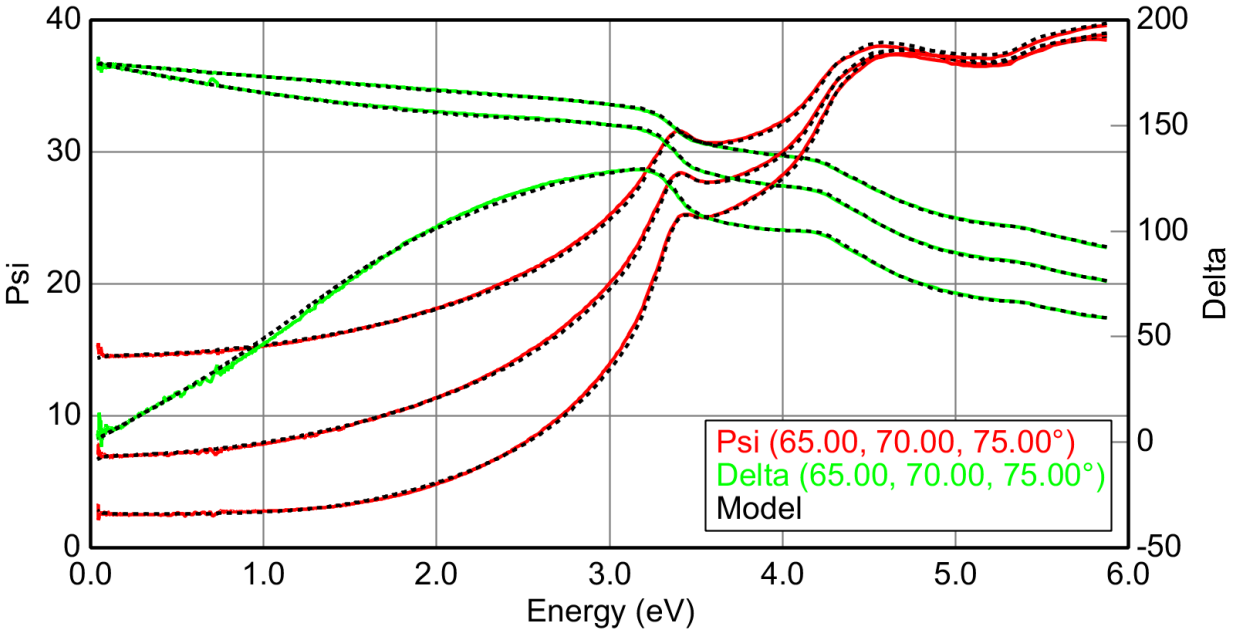

Figure S17. Measured and modelled ellipsometry angles for the sample with a-LAO on a (111) silicon substrate at incident angles of 65°, 70° and 75°.

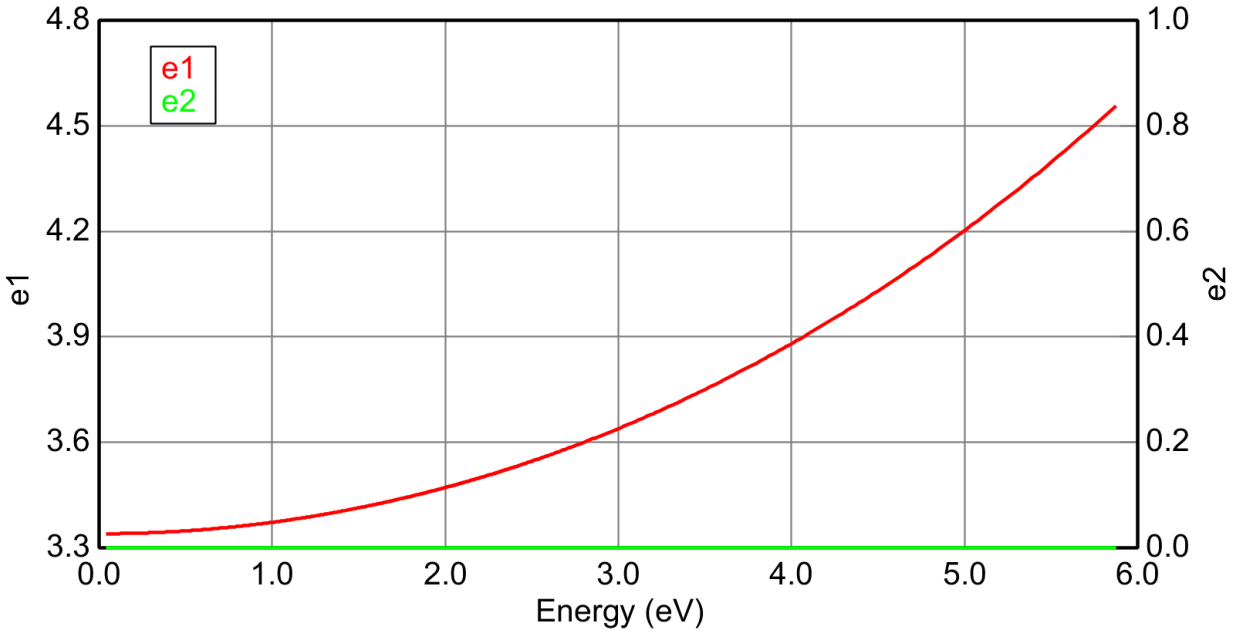

Figure S18. Real (e1) and imaginary parts (e2) of the dielectric functions of the a-LAO layer for the sample with a-LAO on a (111) silicon substrate.

4.4. $Ca_2Nb_3O_{10}^-$ nanosheets

Nanosheets of $Ca_2Nb_3O_{10}^-$ (CNO NS) were deposited by the LB method onto the same (111) silicon substrate previously characterized, in order to determine their DFs.

The absorption spectra of a colloidal suspension of K^+ $Ca_2Nb_3O_{10}^-$ nanosheets (NS) has been measured e.g. by Liang *et al.*[17], who determined a gap energy of 3.38 eV (366 nm) and an absorption maximum at 4.59 eV (270 nm). The absorption spectra of CNO NS deposited onto a transparent substrate (but not by the LB method) has been studied by Xu *et al.*[18]. However, it seems that no direct investigation of the DFs of CNO NS deposited by the LB method by spectroscopic ellipsometry has been reported so far. Therefore, the DFs of the NS cannot be compared to literature data but have to be determined experimentally. They are supposed to be similar to the DFs of their bulk counterpart $KCa_2Nb_3O_{10}$, which can be found e.g. in ref.[19]: the imaginary part ε_2 should be negligible below the gap energy, and the real part ε_1 should be close to 4. The NS are found to be transparent with an optical index $n \approx 2$.

4.4.1. Determination of the thickness

In order to extract the thickness of the film, a simple Cauchy model is used for the NS, while the fitting procedure is restricted to a wavelength range in which the NS are completely transparent, from 0.15 to 2.48 eV (500 to 8 000 nm). The simultaneous fitting of the thickness and the parameter A and B allows the determination of a thickness of 3.3 nm, while the fitted value of $A = 2.065$ indicates an optical index indeed close to 2.

The thickness of a single CNO sheet is close to 1.6 nm. We can therefore conclude that the NS layer has an average of 2 single layers of CNO sheet. In fact, to prepare these samples, the LB method was repeated 3 times until a satisfying coverage is attained, but each deposition does not provide a complete coverage, so an average coverage of 2 CNO sheet is absolutely plausible.

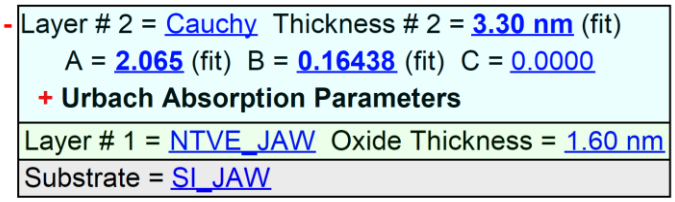

Figure S19. Optical model for the sample with NS on a (111) silicon substrate in their transparent region.

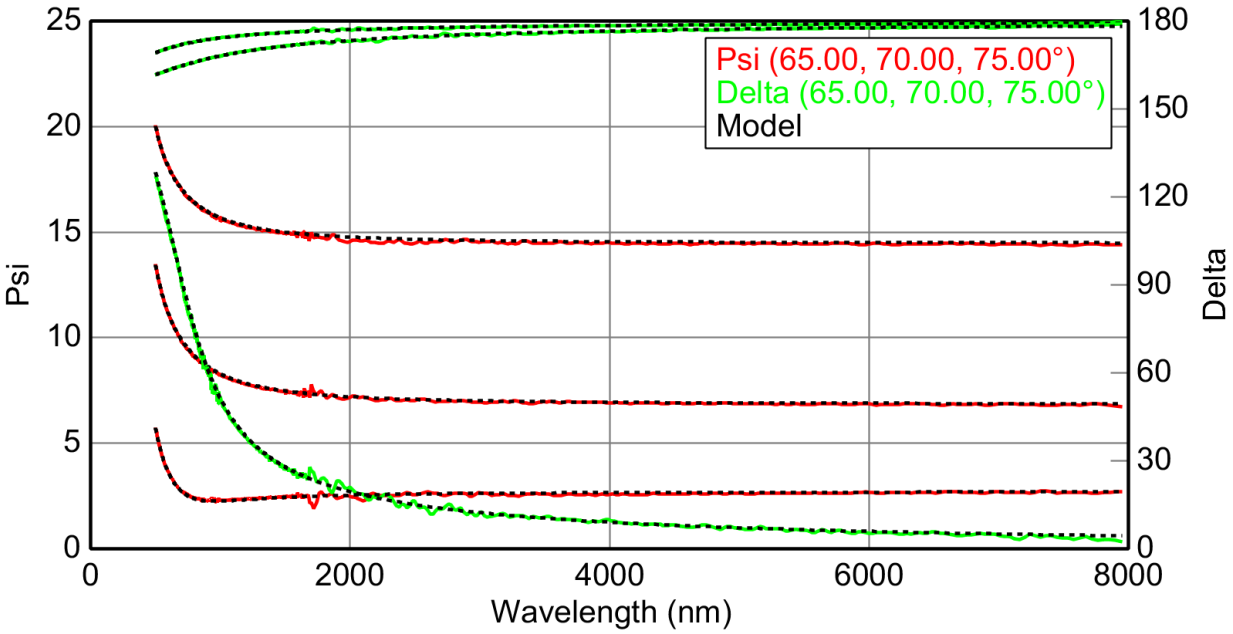

Figure S20. Measured and modelled ellipsometry angles for the sample with CNO NS on a (111) silicon substrate in their transparent region.

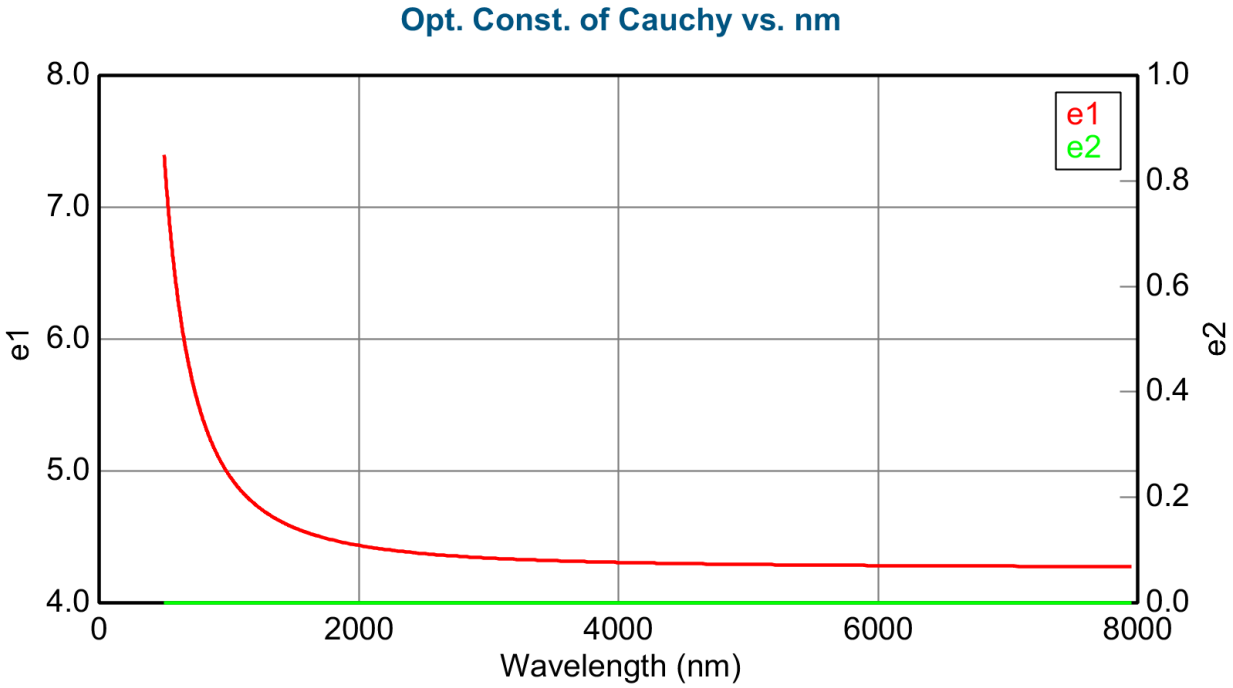

Figure S21. Dielectric functions of the NS layer for the sample with CNO NS on a (111) silicon substrate in their transparent region.

4.4.2. Determination of the dielectric functions: Wavelength-by-wavelength fit

The thickness of the NS being fixed to 3.3 nm, it is possible to calculate the DFs ε_1 and ε_2 of the NS for each given wavelength in the whole spectral range, which is called a Wavelength-by-wavelength fit.

The results are displayed on figure S27. The DFs extracted by the Wavelength-by-wavelength procedure are rather noisy, which is typical for this method as no correlation is assumed between the neighbouring wavelength points. All the noise coming from the measurement and the limits of the modelling procedure impacts the DFs values. A maximum of ε_2 around 5 eV is clearly identified, and the NS layer is rather transparent below 3 eV, which is consistent with ref.[17]. However, the DFs in the transparent region are surprising: instead of a transparent film with $\varepsilon_1 \approx 4$ and $\varepsilon_2 \approx 0$ below the gap of 3.38 eV as expected for CNO NS from the literature, we extract a rather high $\varepsilon_2 \approx 0.5$ value.

However, as mentioned previously, the LB method was repeated 3 times until a satisfying coverage is reached. Therefore, the restacking between consecutive NS layers may induce a sizeable porosity. The NS have a typical width of a few micrometers which is close to the wavelength of the probing light. This can induce porosities which can lead to non-specular diffuse scattering.

This diffuse scattering may be Rayleigh-type diffusion ($\sim 1/\lambda^4$) or similar tendency diffusion, typically decreasing as a power-law of the inverse of the wavelength. This has been previously mentioned by Xu *et al.*[18], who observed similar strong diffuse scattering in NS films of various thicknesses deposited onto a transparent substrate.

The standard spectroscopic ellipsometry measurement technique used here does not allow to distinguish between absorption and diffuse scattering: non-specular reflection is hence interpreted in the Wavelength-by-wavelength fit as a non-physical high value of ε_2. It is also to be mentioned that spectroscopic ellipsometry in reflection configuration often tends to overestimate the absorption, so that the values of ε_2 of our sample might actually be lower than the ones extracted here.

4.4.3. Effective medium model for the $Ca_2Nb_3O_{10}^-$ NS layer

It is highly desirable to remove the unphysical noise of the Wavelength-by-wavelength procedure, and to provide a physical description of the DFs of the NS layer. For this, we build an optical model with continuous functions like oscillators for the NS on one hand, and take the porosity into account by an Effective Medium Approximation (EMA) on the other hand.

4.4.3.1. Oscillator model for the $Ca_2Nb_3O_{10}^-$ NS

Consistently with the DFs of bulk $KCa_2Nb_3O_{10}$ obtained by *ab initio* calculation by Virdi *et al.*[19], we chose to model the DFs of the NS by the contribution of 2 oscillators:

(1) A Tauc-Lorentz oscillator to represent the direct gap. Following Liang *et al.*[17], we chose a gap energy E_g = 3.38 eV and a maximum of absorption at E_0 = 5.59 eV.

(2) A Gaussian oscillator arbitrarily centered at 8 eV to represent the others interband transitions taking place in the UV, out of the measurement range, that may induce dispersion below 6 eV.

We also add a value ε_∞ to the real part of the DFs in order to model the dispersion stemming from further interband transitions at even higher energy. The amplitudes and width of these oscillators, as well as the value of ε_∞, are modified manually to match approximately the DFs of ref.[19]: specifically, we ensure ε_1 = 4 and ε_2 = 0 below the gap energy.

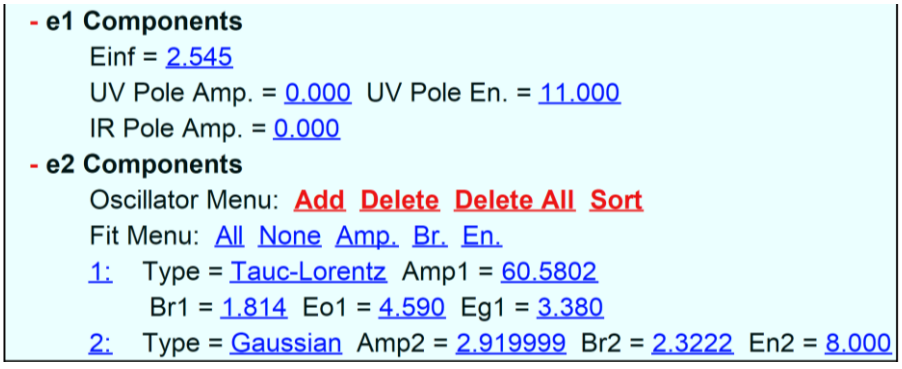

Figure S22. Oscillators model used for the CNO nanosheets.

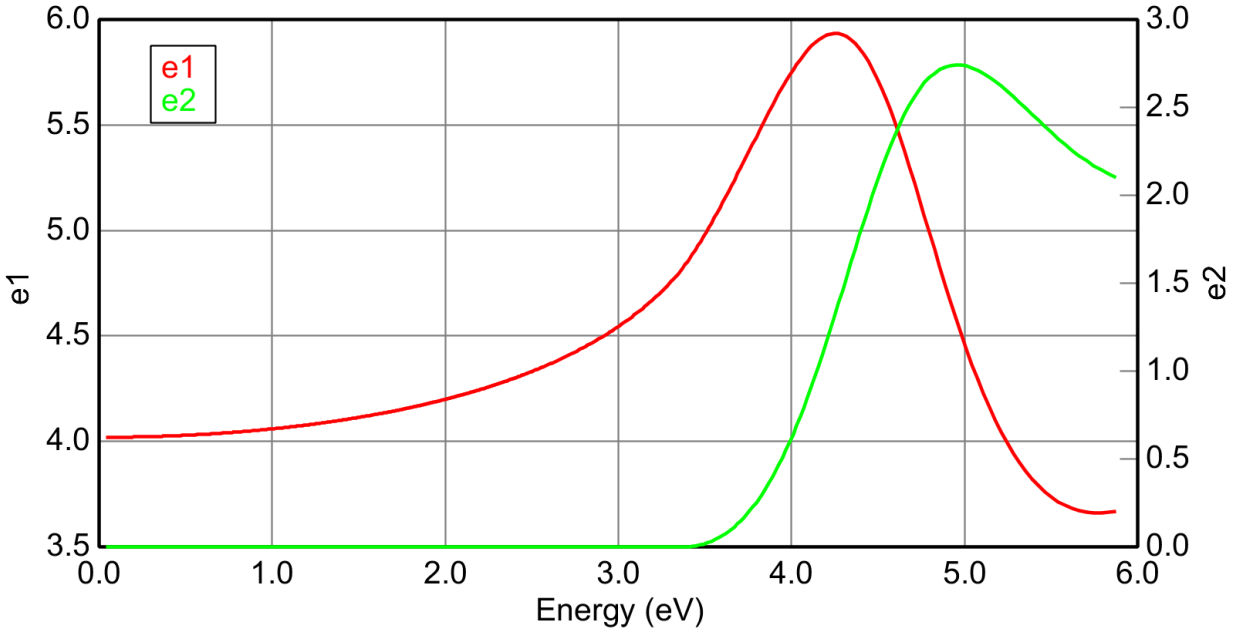

Figure S23. Dielectric functions of the oscillators' model used for the CNO nanosheets.

4.4.3.2. Effective medium approximation for the $Ca_2Nb_3O_{10}^-$ NS layer

We can now model the NS layer by an effective medium approximation (EMA), which is a porous structure made of two materials:

(1) The pristine NS, which DFs are the ones obtained with the oscillators' model in the previous section (figures S22 and S23).

(2) The air filling the porosity. Its optical indexes are represented by a Cauchy model, with $n = 1$ for air. Furthermore, an Urbach absorption tail is added in order to represent the artificial absorption due to diffuse scattering (figures S24 and S25), which is defined by: $k = k\ Amplitude \cdot e^{exponent \cdot (E - Band\ Edge)}$.

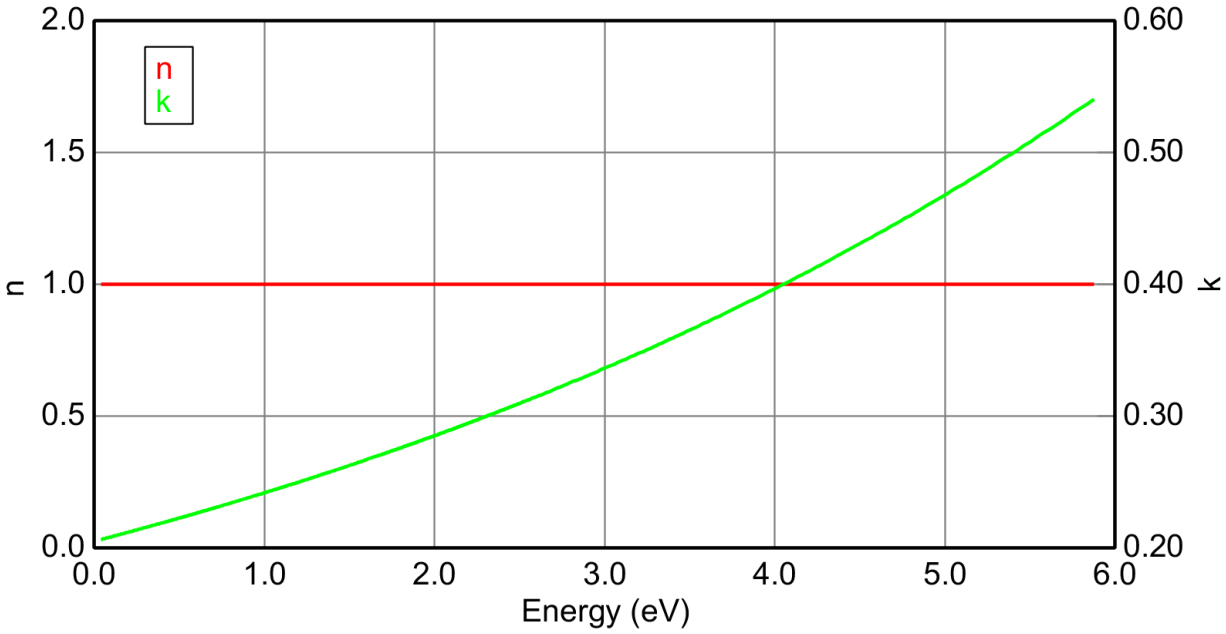

Figure S24. Optical indexes of the Cauchy model with Urbach absorption tail used for the porous inclusions.

This procedure has been successfully applied to include the effect of diffuse scattering in porous structures by Maudet *et al.*[20]. The advantage here is that we keep Kramers-Kronig consistency for the DFs of the NS. Diffuse scattering, which is a non-Kramers-Kronig consistent process, is taken into account via an Urbach absorption law, which is indeed not Kramers-Kronig consistent. Urbach absorption law is suitable to represent diffuse scattering processes which vary as a power-law of the inverse of the wavelength (Rayleigh-type ($\sim 1/\lambda^4$), or similar processes). On the contrary, attributing the seemingly high dielectric losses to a high value of ε_2 of the NS themselves would have no physical meaning.

These two materials are then combined through the Bruggeman Effective Medium Approximation (Bruggeman EMA) to obtain the effective DFs of the NS layer. As the NS are two-dimensional objects and the film is very thin, we can apply a two-dimensional Bruggeman EMA, with a depolarization factor of 0.5 (suitable for circular inclusion in 2D, as the film is isotropic within the plane of the substrate).

As the thickness of the NS layer and the DFs of the NS are fixed, the only fitting parameters are therefore the $k\ Amplitude$ and the $exponent$ of the Urbach law, and the level of $Porosity$, as shown on figure S25. The resulting DFs for the NS layer are shown on figure S27. As one can see, they are very similar to those obtained by the Wavelength-by-

wavelength fit procedure, with the advantage of providing a smoother energy dependence for the DFs.

- Layer # 2 = EMA Thickness # 2 = 3.30 nm
  - # of Constituents = 2
  - Material 1 = NS TL G
    - Show Dialog
    - **e1 Components**
      - Einf = 2.545
      - UV Pole Amp. = 0.000 UV Pole En. = 11.000
      - IR Pole Amp. = 0.000
    - **e2 Components**
      - Oscillator Menu: Add Delete Delete All Sort
      - Fit Menu: All None Amp. Br. En.
      - 1: Type = Tauc-Lorentz Amp1 = 60.5802
        Br1 = 1.814 Eo1 = 4.590 Eg1 = 3.380
      - 2: Type = Gaussian Amp2 = 2.919999 Br2 = 2.3222 En2 = 8.000
  - Material 2 = Cauchy
    - A = 1.000 B = 0.0000 C = 0.0000
    - **Urbach Absorption Parameters**
      - k Amplitude = **0.39659** (fit) Exponent = **0.165** (fit)
      - Band Edge = 4.000 eV
  - Porosity (%) = **41.5** (fit)
  - depolarization = 0.500 Analysis Mode = Bruggeman
- Layer # 1 = NTVE_JAW Oxide Thickness = 1.60 nm
- Substrate = SI_JAW

Figure S25. Optical model for the sample with NS on a (111) silicon substrate with the Bruggeman EMA model for the NS layer.

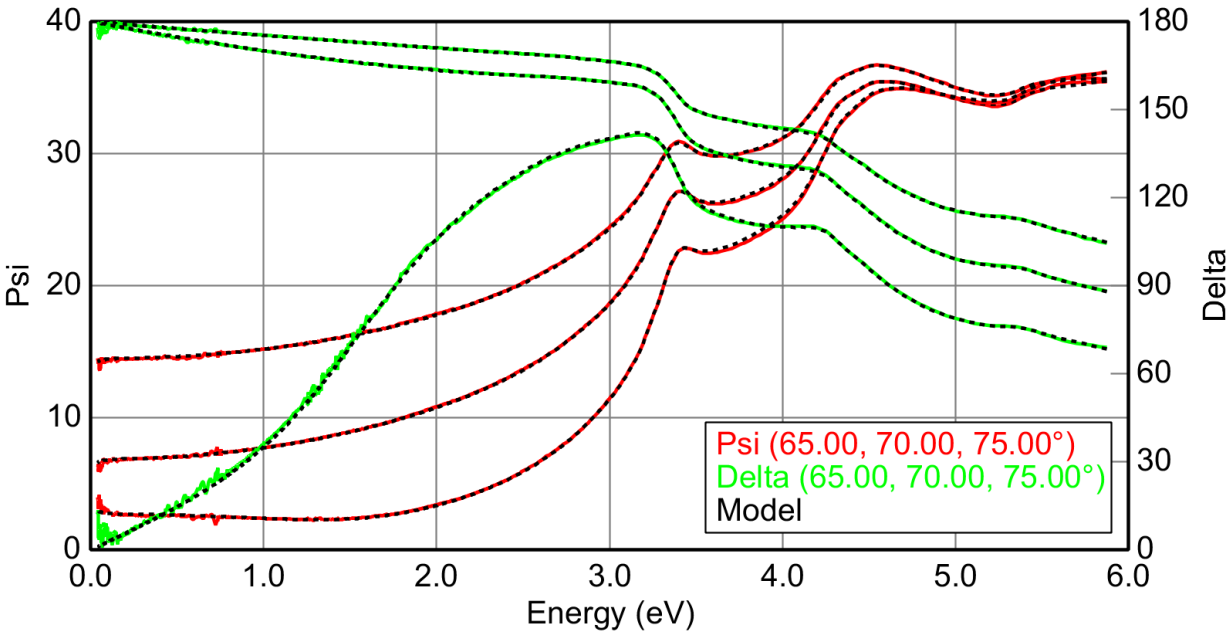

Figure S26. Measured and modelled ellipsometry angles for the sample with NS on a (111) silicon substrate with the Bruggeman EMA model for the NS layer.

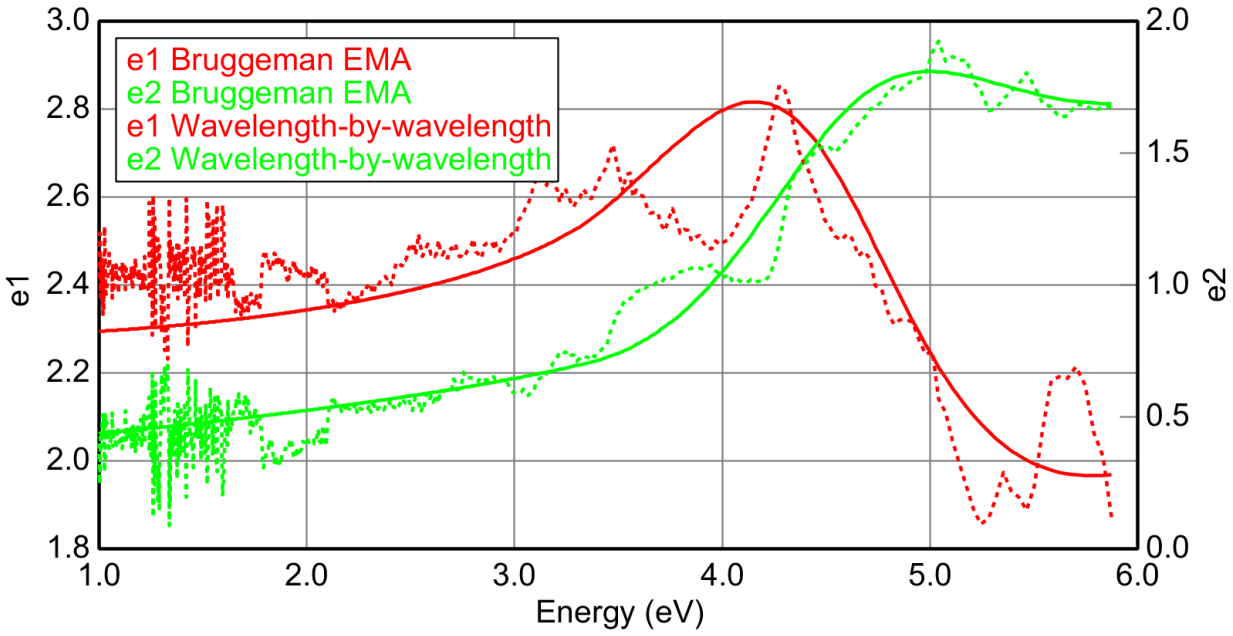

Figure S27. Dielectric functions of the NS layer with Bruggeman EMA (thick line). The DFs obtained by the Wavelength-by-wavelength fit are shown as dash lines for comparison.

4.5. Eagle XG Corning® glass substrate

A pristine Eagle XG Corning® glass substrate is studied in order to determine its DFs. As it is double-side polished, the back reflections are suppressed by applying 3M Scotch® Magic™ tape on the back side of the substrate. Indeed, as the optical index of the tape is close to the one of silica ($n \sim 1.5$), there is no reflection at the interface between the silica and the tape. Then, the matte-finish of the tape ensures the diffuse scattering of all the incoming light. It has been checked that, by applying this method, the line-of-sight transmitted light is indeed negligible, and the depolarization in reflection configuration is less than 3 % from 0.2 eV to 6 eV. Therefore this method provides an efficient roughening of the backside of the substrate.

As the thickness of 0.5 mm of the substrate is known, we can perform a Wavelength-by-wavelength fit of the DFs. The obtained DFs are afterwards fitted by a model comprising several oscillators in order to smooth out the experimental and modelling noise present with the Wavelength-by-wavelength procedure. A Sellmeier pole is used to model the high-energy dispersion on the UV side, and a series of Gaussian oscillators are used to model the infrared

absorption peaks present below 0.2 eV. The optical model, ellipsometry angles and corresponding DFs are shown on figures S28, S29 and S30 respectively.

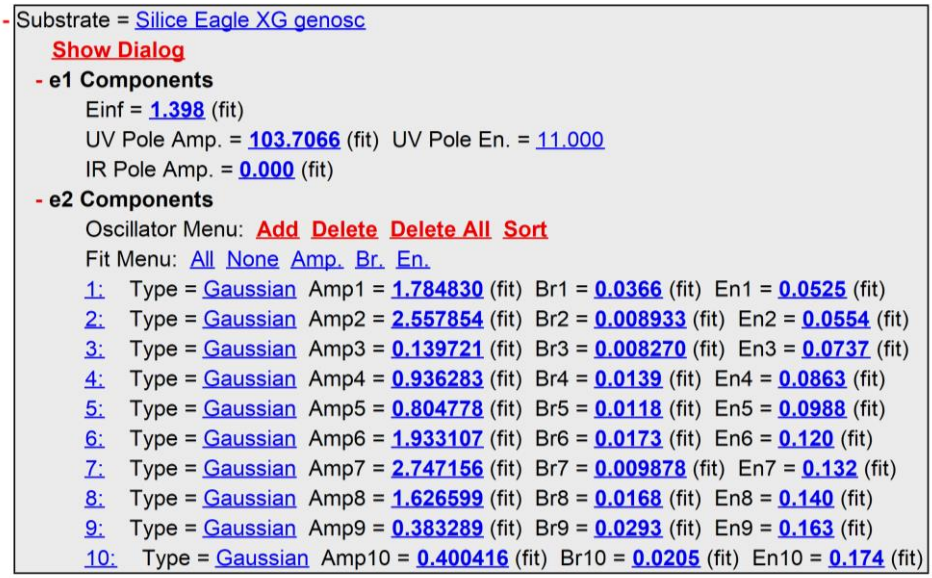

Figure S28. Optical model for the Eagle XG Corning® glass substrate.

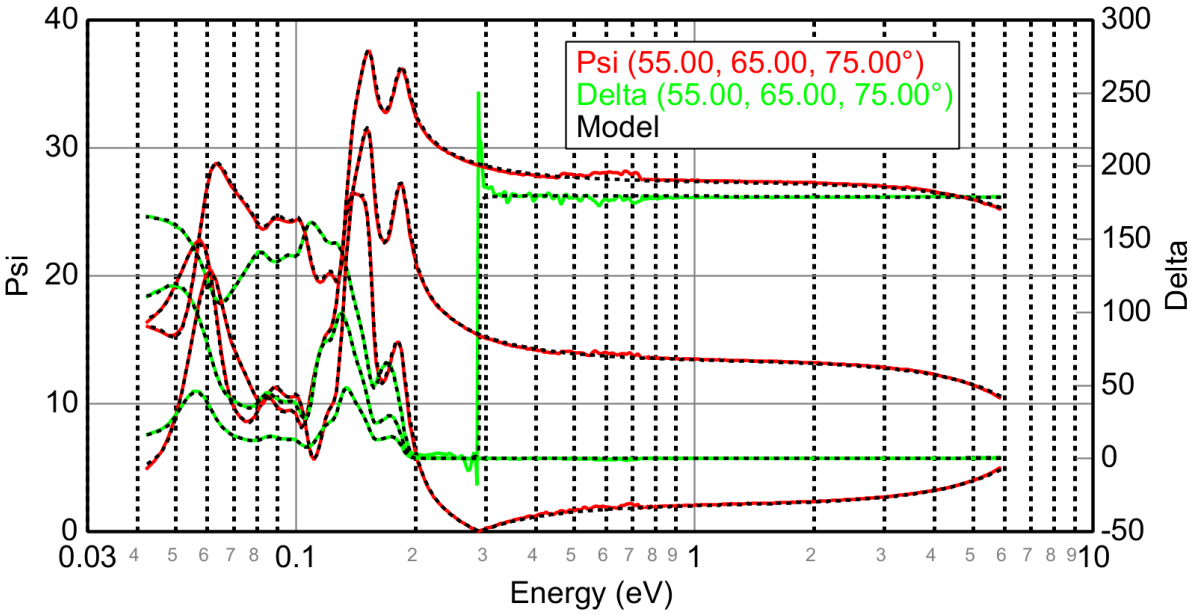

Figure S29. Measured and modelled ellipsometry angles for the Eagle XG Corning® glass substrate with the oscillators model.

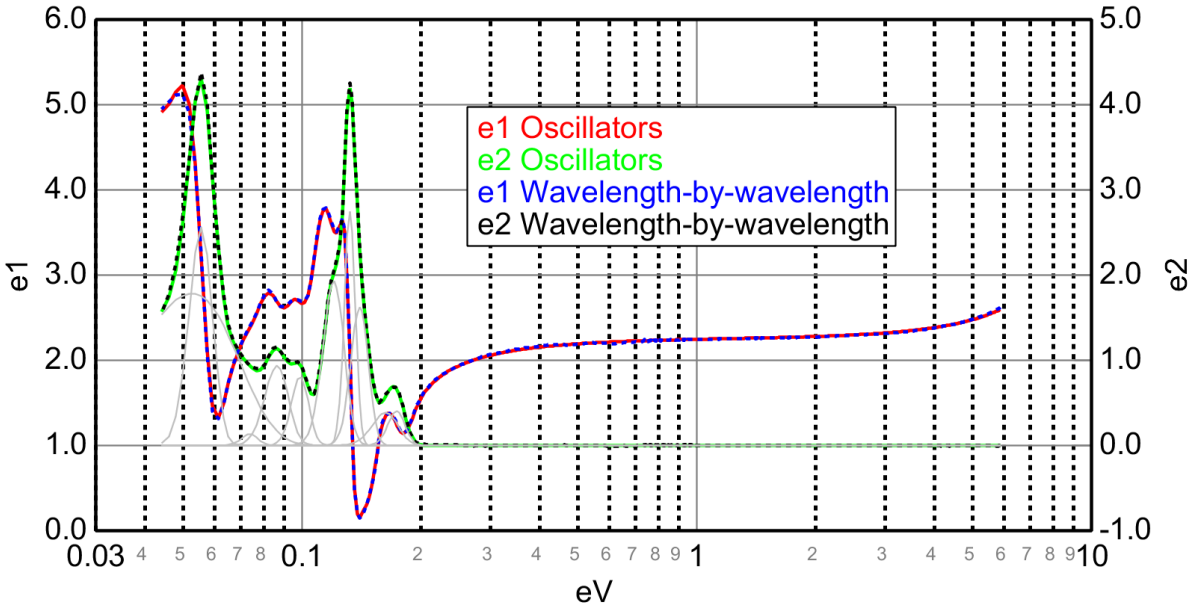

Figure S30. Dielectric functions of the Eagle XG Corning® glass substrate with the oscillators model (red and green lines). The grey thin lines represent the contribution of each oscillator. The dielectric functions obtained by the Wavelength-by-wavelength fit are shown for comparison (blue and black dotted lines).

4.6. $CaVO_3$ and $SrVO_3$ layers

The sample of interest is composed of several layers: the figure S15 summarizes the scheme of the complete sample stacking.

When the DFs and thicknesses of all the other layers are determined, it is possible to investigate the DFs of the CVO (SVO) layer. The precise average thickness of this layer has been determined by X-Ray Reflection (XRR) measurement and will thus be fixed to this value.

As mentioned before, the coverage of the NS on the substrate is lower than 100 %. CVO or SVO can crystallize only if it grows epitaxially onto the nanosheets. If it grows directly onto the substrate, it will remain amorphous. Therefore, an effective medium model should be built to take into account the proportion of amorphous CVO or SVO present in the layer. In the following, we will present the method for the CVO series, as the method is identical the SVO series.

4.6.1. Amorphous $CaVO_3$: sample CVO 400 °C

4.6.1.1. Wavelength-by wavelength fit

At the deposition temperature of 400 °C, the CVO (SVO) layer is almost completely amorphous, as shown by the X-ray diffraction measurements. Therefore, the CVO (SVO) layer can be modelled as an isotropic homogeneous layer, and a Wavelength-by-wavelength fit can be performed, as its thickness is known from XRR measurement (40.2 nm for CVO 400 °C). The resulting DFs are shown on figure S33.

4.6.1.2. Oscillator model

In order to smooth out the noise of the Wavelength-by-wavelength fit, an oscillator model is then built for the sample CVO 400 °C. Following the spectroscopic ellipsometry measurement and the *ab initio* calculation for $CaVO_3$ and $SrVO_3$ from Zhang *et al.*[6], we include the following oscillators:

(1) A Tauc-Lorentz oscillator with an energy gap E_g = 2.773 eV and a maximum of absorption at E_0 = 3.902 eV in order to represent the direct band gap absorption peak due to the interband transitions from the *2p* to the t_{2g} orbitals, as detailed in ref.[6].

(2) A Drude oscillator to represent the absorption due to the free carriers, that is, the intraband transitions within the t_{2g} band.

(3) A Gaussian oscillator arbitrarily centered at 8 eV to represent the others interband transitions taking place in the UV, out of the measurement range, that may induce absorption and dispersion below 6 eV.

(4) A Gaussian oscillator around 2 eV to model the t_{2g} to e_g interband transitions.

We also add a constant value ε_∞ to the real part of the DFs in order to model the dispersion stemming from further interband transitions at even higher energy. The amplitudes'widths and energies of all these oscillators, as well as ε_∞, are first fitted onto the DFs obtained by the Wavelength-by-wavelength fit (firstly through a manual procedure, and secondly by numerical fitting), and then fitted again directly onto the measured ellipsometry angles. The full optical model, ellipsometry angles and resulting DFs are shown on figures S31, S32 and

S33, respectively. The agreement between experimental and modelled ellipsometry angles is very good, with a low value of *MSE* = 3.355.

+ Layer # 3 = LAOa Cauchy Thickness # 3 = 5.40 nm
- Layer # 2 = cvo 191213 400degC visir - TL GGG D Thickness # 2 = 40.20 nm
  Show Dialog
  - **e1 Components**
    Einf = **1.238** (fit)
    UV Pole Amp. = 0.000 UV Pole En. = 11.000
    IR Pole Amp. = 0.000
  - **e2 Components**
    Oscillator Menu: Add Delete Delete All Sort
    Fit Menu: All None Amp. Br. En.
    1: Type = Tauc-Lorentz Amp1 = **47.5488** (fit)
    Br1 = **1.618** (fit) Eo1 = **3.902** (fit) Eg1 = **2.773** (fit)
    2: Type = Drude(RT) Resistivity (Ohm·cm)2 = **0.002231** (fit) Scat. Time (fs)2 = **0.381** (fit)
    3: Type = Gaussian Amp3 = **4.742767** (fit) Br3 = **4.7349** (fit) En3 = 8.000
    4: Type = Gaussian Amp4 = **0.644681** (fit) Br4 = **8.5239** (fit) En4 = **2.173** (fit)
+ Layer # 1 = NS EMA TLG - Urbach Thickness # 1 = 3.30 nm
+ Substrate = Silice Eagle XG visir genosc fit

Figure S31. Optical model for the sample CVO 400 °C with the oscillators' model.

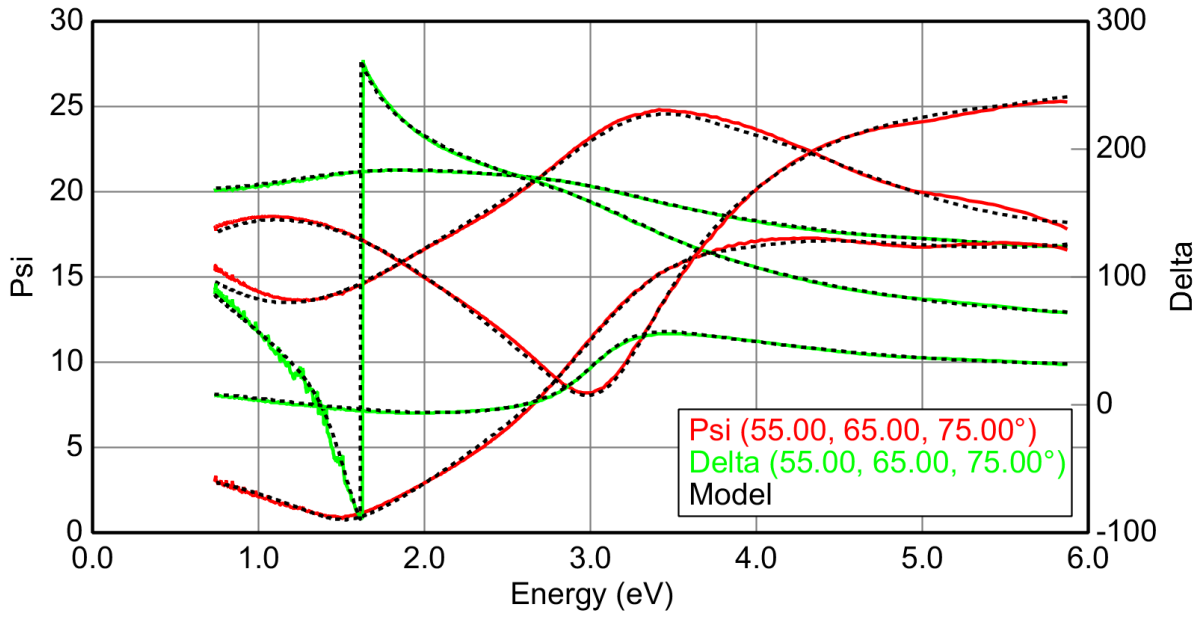

Figure S32. Measured and modelled ellipsometry angles for the sample CVO 400 °C with the oscillators' model.

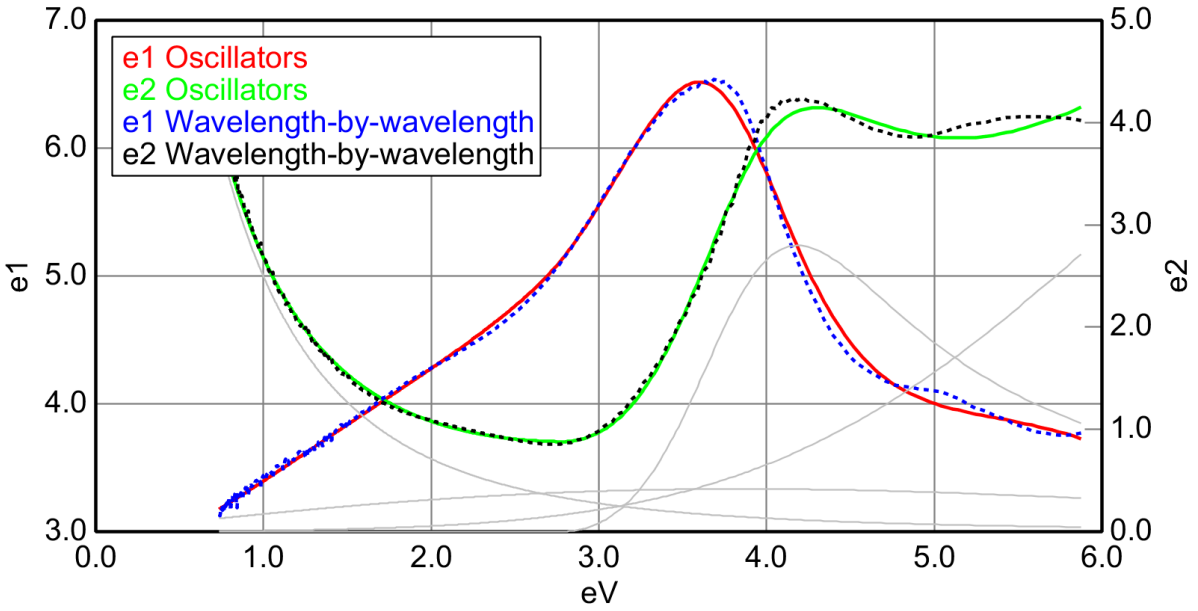

Figure S33. Dielectric functions of amorphous $CaVO_3$ (sample CVO 400 °C) with the oscillators' model (red and green plain lines). The grey thin lines represent the contribution of each oscillator. The dielectric functions obtained by the Wavelength-by-wavelength fit are shown for comparison (blue and black dashed lines).

4.6.2. Crystalline $CaVO_3$: sample CVO 500 °C

We now investigate the DFs of the sample CVO 500 °C, which is nicely crystallized as determined from the X-ray diffraction measurement.

The amorphous CVO incorporated inside the CVO-SVO layer is supposed to have the same DFs as the CVO 400 °C sample determined in the previous section. The presence of NS underneath the layer determines the crystalline or amorphous character of the CVO growing on the top of it throughout all the thickness of the film. Therefore, as the film is much thinner (40 nm) than the width of the NS (several micrometers), the amorphous and crystalline inclusions have a highly oblate aspect ratio, and thus can be approximated as flat cylinders in a three-dimensional medium. This is modelled in the framework of the Anisotropic Bruggeman Effective Medium Approximation (ABEMA) by a depolarization factor $L_z = 1$ in the perpendicular direction of the substrate (z direction), and an isotropic behaviour within the plane of the substrate ($L_x = L_y = 0.5$, i.e., *x-y split* equal to 0.5). Therefore, the only fitting parameter of this ABEMA scheme is the proportion of the amorphous phase $P_{amorphous}$.

Following ref.[6], the crystalline CVO is modelled very similarly to the amorphous CVO by the following oscillators:

(1) A Tauc-Lorentz oscillator with an energy gap E_g = 2.553 eV and a maximum of absorption at E_0 = 3.422 eV in order to represent the direct band gap absorption peak due to the interband transitions from the *2p* to the t_{2g} orbitals, as detailed in ref.[6].

(2) A Drude oscillator to represent the absorption due to the free carriers, i.e. the intraband transitions within the t_{2g} band.

(3) A Gaussian oscillator arbitrarily centered at 8 eV to represent the others interband transitions taking place in the UV, out of the measurement range, that may induce absorption and dispersion below 6 eV.

(4) A Gaussian oscillator around 5 eV to model the other UV interband transitions within the measurement range.

(5) A Gaussian oscillator around 1 eV to model the t_{2g} to e_g interband transitions.

We also add a constant value ε_∞ to the real part of the DFs in order to model the dispersion stemming from further interband transitions at even higher energy.

As a first step, the amplitudes, widths and energies of all these oscillators, as well as ε_∞, are fitted onto the measured ellipsometry angles while assuming $P_{amorphous}$ = 0 %. In this case, the ABEMA model reduces to an isotropic model for the CVO (SVO) layer, i.e. exactly the same model as the one used successfully for the amorphous sample CVO 400 °C. However, we obtain a value of *MSE* = 6.040, which is twice higher than the CVO 400 °C sample. From a visual point of view, the fit does not look good neither (blue dashed line on figure S35). Other attempts to improve the model, like adding more oscillators to the model, have also resulted in a fit of poor quality.

The failure of the isotropic model ($P_{amorphous}$ = 0 %) demonstrates the need to include the amorphous CVO domains within the ABEMA model, which is anisotropic. The amplitudes, widths and energies of all these oscillators, as well as ε_∞, are now fitted together with the additional parameter $P_{amorphous}$. The starting values for the oscillators are the ones obtained previously by the isotropic model, and the starting value for $P_{amorphous}$ is 0 %. The quality of the fit is substantially improved by including a proportion of $P_{amorphous}$ = 30.2 % of amorphous CVO (SVO) into the CVO (SVO) layer, with a strong reduction of 38 % of the *MSE* down to 3.752, as can be seen on figure S35. The same difficulty in the fitting procedure was observed for all the samples of the CVO and SVO series grown at 500, 600 and 700 °C, with similar

MSE improvement once the ABEMA scheme is applied. The extracted values for $P_{amorphous}$ in the framework of the anisotropic ABEMA model are summarized in table S3.

Considering the anisotropic approach, the percentage of crystallized volume $P_{crystallized}$ = 100 – $P_{amorphous}$, as measured by SE, and the percentage of surface coverage by the NS ($P_{coverage}$) determined by microscopy, converge together toward the same value for all samples (~ 70 %, see table S1 and figure 1 (f) in the main text), which means that the SE and microscopy measurements are in good accordance, enforcing the validity of the ABEMA model. The conclusion is that the built anisotropic effective model is validated and takes into account precisely the microstructure of the layered samples. The second point is the possibility to determine easily the surface coverage by SE analysis and confirming the important coverage of the surface reached thanks to the LB dip-coating method.

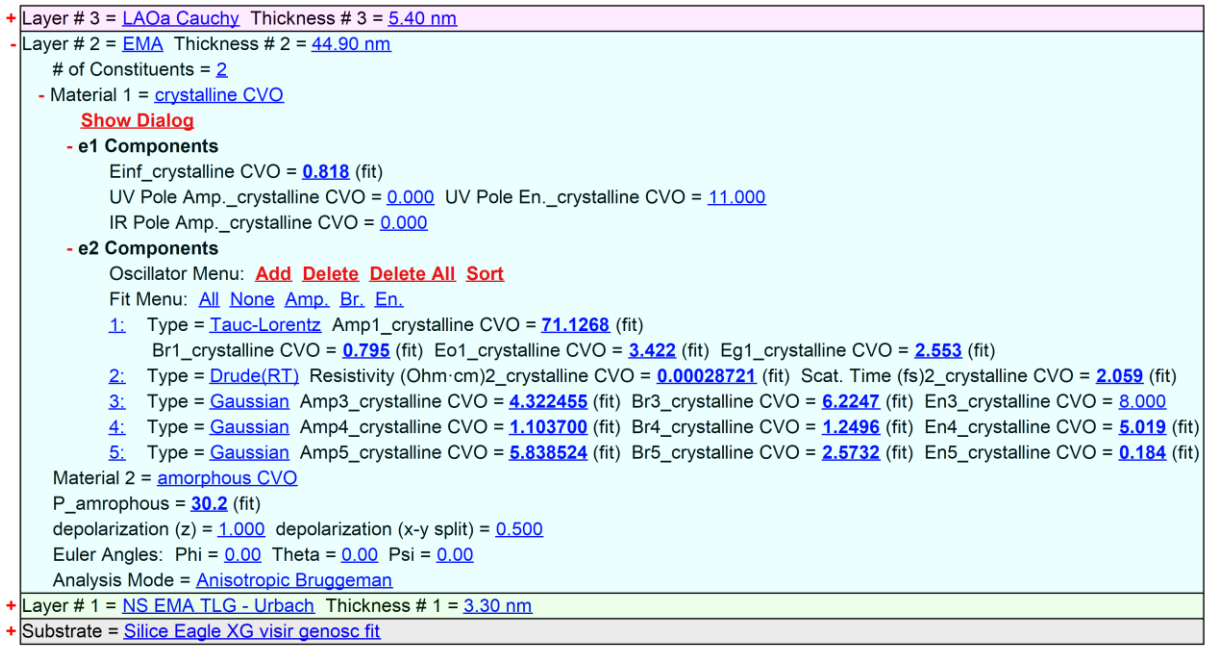

Figure S34. Optical model for the sample CVO 500 °C with the ABEMA model.

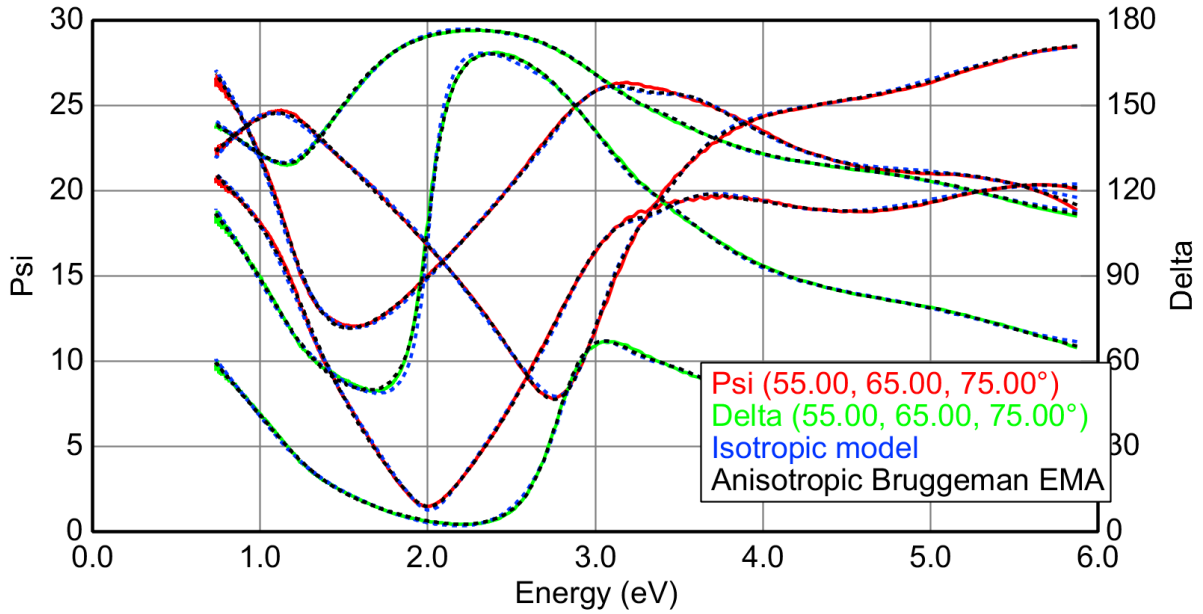

Figure S35. Measured (red and green) and modelled ellipsometry angles for the sample CVO 500 °C with the ABEMA model (black dashed line, *MSE* = 3.752). The fit with the isotropic model is also shown for comparison (blue dashed line, *MSE* = 6.040).

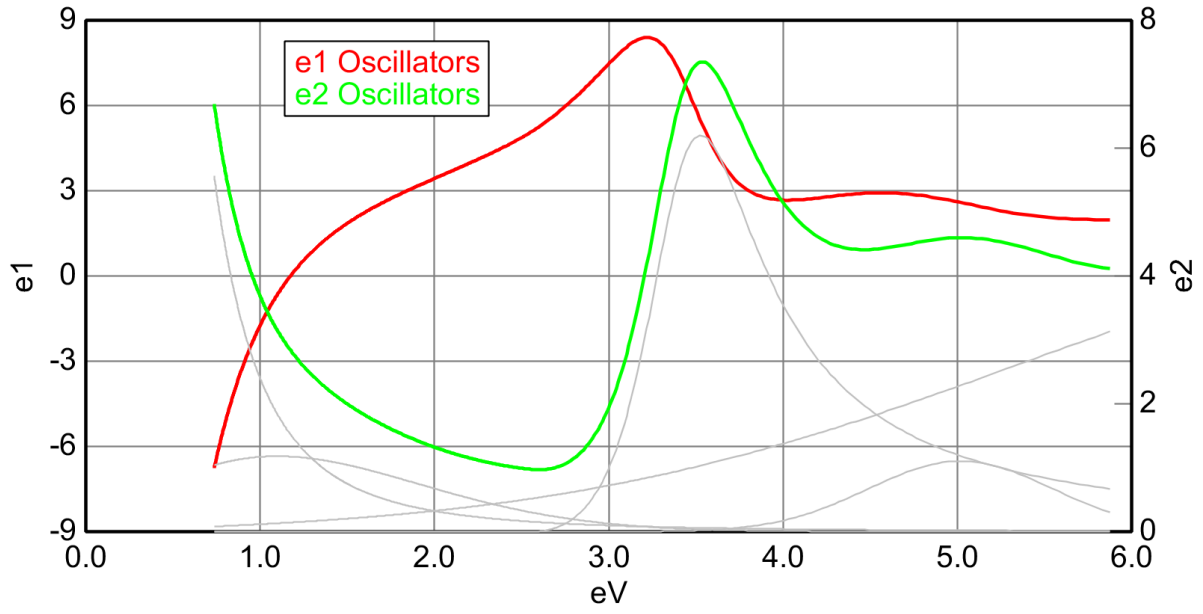

Figure S36. Dielectric functions for the crystallized CVO inside the CVO (SVO) layer of the sample CVO 500 °C with the oscillators model and the ABEMA scheme (red and green lines). The grey thin lines represent the contribution of each oscillator.

4.7. Infrared properties of the $CaVO_3$ and $SrVO_3$ layers

CVO and SVO perovskites exhibit strong electron-electron correlations. It is well known that this results to an enhancement of the effective mass, and also affects the dielectric properties in several manners; in particular, for the free carriers, a deviation from the simple Drude model is observed in the infrared range, and a generalized Drude model analysis can be applied instead of investigating the behaviour of the free carriers, as demonstrated by Makino *et al.*[13]. In this approach, the effective mass m^* and scattering rate γ are not taken as constant values anymore like in the simple Drude model, but rather considered as frequency-dependant functions $m^*(\omega)$ and $\gamma(\omega)$. The DFs have been determined by a Wavelength-by-wavelength fit in order to extract the spectral functions $m^*(\omega)$ and $\gamma(\omega)$ through the generalized Drude model analysis.

For this reason, in the previous section, we restricted the analysis of the CVO (SVO) layer to the NIR-vis-UV region (0.7 to 5.9 eV), where the free carriers do not yet dominate the shape of the DFs. A simple Drude model was applied there, because the spectral region is restricted to the near infrared (NIR), so that the effective mass m^* and scattering rate γ can indeed be considered as constant on this reduced spectral range.

We mention here that the "optical" resistivity ρ_{opt}, mobility μ_{opt}, scattering time τ_{opt} and carrier density N_{opt} presented in the main text are the ones extracted by this simple Drude model restricted to the NIR range. On the other hand, the generalized Drude analysis was used to extract the plasma frequencies ω_p and the effective masses m^*.

Thus, the DFs in the NIR-vis-UV range, as well as the structural and ABEMA parameters (thickness, proportion of amorphous phase, and depolarization factors), which are independent of the wavelength, has been determined and validated by using oscillator functions with a simple Drude model for energies above 0.7 eV.

4.7.1. Wavelength-by-wavelength fit

As a result, we can now set these structural parameters and perform a Wavelength-by-wavelength fit for the crystalline part of the CVO (SVO) layer in order to proceed to the generalized Drude model analysis: this time, the fit is extended to the IR range at energies

below 0.7 eV. The full optical model, ellipsometry angles and resulting DFs are shown on figures S37, S38 and S39, respectively.

+ Layer # 3 = LAOa Cauchy Thickness # 3 = 5.40 nm
- Layer # 2 = EMA Thickness # 2 = 44.90 nm
  # of Constituents = 2
  + Material 1 = crystalline CVO - Wavelength-by-wavelength fit
  Material 2 = amorphous CVO
  P_amorphous = 30.2
  depolarization (z) = 1.000 depolarization (x-y split) = 0.500
  Euler Angles: Phi = 0.00 Theta = 0.00 Psi = 0.00
  Analysis Mode = Anisotropic Bruggeman
+ Layer # 1 = NS EMA TLG - Urbach Thickness # 1 = 3.30 nm
+ Substrate = Silice Eagle XG visir genosc fit

Figure S37. Optical model for the sample CVO 500 °C with the ABEMA + Wavelength-by-wavelength fit.

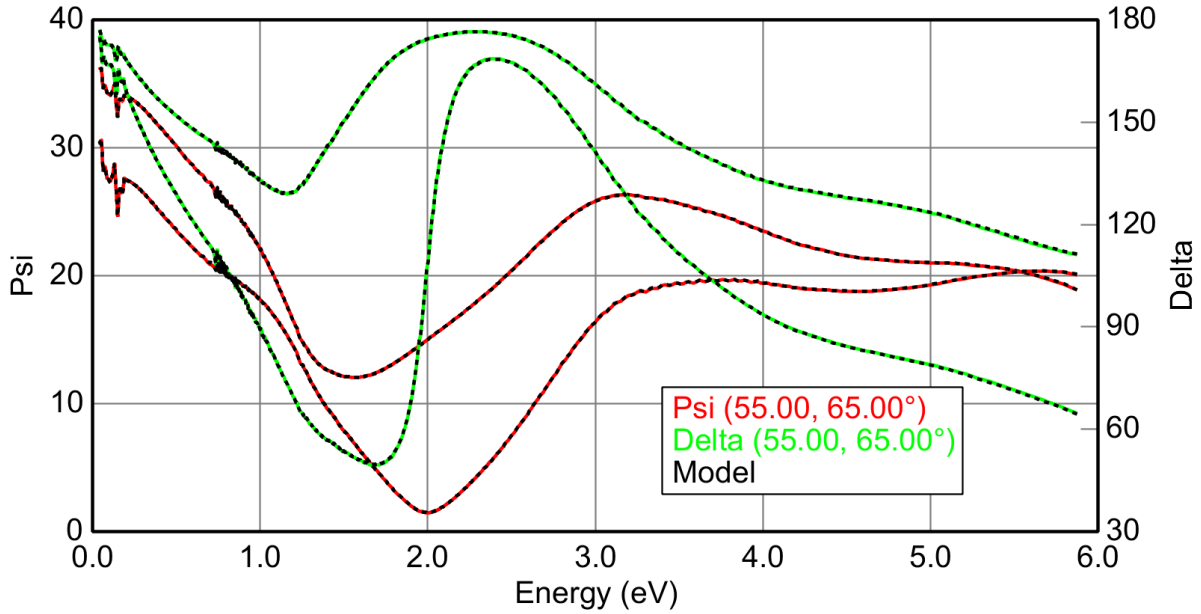

Figure S38. Measured and modelled ellipsometry angles in the IR to UV range for the sample CVO 500 °C with the ABEMA + Wavelength-by-wavelength fit.

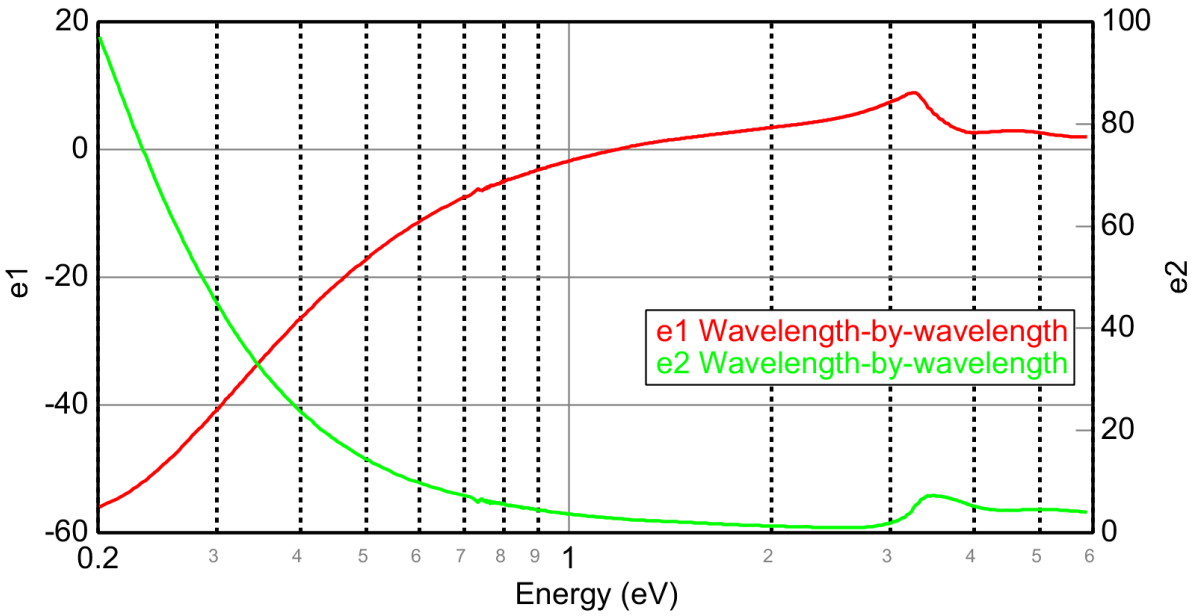

Figure S39. Dielectric functions in the IR to UV range for the crystallized CVO inside the CVO (SVO) layer of the sample CVO 500 °C with the ABEMA + Wavelength-by-wavelength fit.

4.7.2. Generalized Drude model analysis

4.7.2.1. Dielectric functions

According to the generalized Drude model[21,22], $\varepsilon(\omega)$ is expressed as:

$$\varepsilon(\omega) = \varepsilon_\infty - \frac{\omega_p^2(\omega)}{\omega^2 + i\omega\gamma(\omega)} \quad \text{(F)}$$

Where the unscreened plasma frequency $\omega_p(\omega)$ is defined as:

$$\omega_p^2(\omega) = \frac{Ne^2}{\varepsilon_0 m_e m^*(\omega)} \quad \text{(G)}$$

Where N is the free carrier density, e the electron charge, ε_0 the permittivity of vacuum, m_e the bare electron mass and m^* the effective mass. N is a constant that is determined from the Hall effect DC measurement.

4.7.2.2.Screened plasma frequency ω_p^*

As soon as the dielectric functions $\varepsilon(\omega) = \varepsilon_1(\omega) + i\varepsilon_2(\omega)$ as a function of the frequency ω has been determined, it is possible to calculate the energy-loss function which is defined as:

$$Im\left[-\frac{1}{\varepsilon(\omega)}\right] = \frac{\varepsilon_2(\omega)}{\varepsilon_1^2(\omega)+\varepsilon_2^2(\omega)} = \frac{\omega_p^2(\omega)\omega\gamma(\omega)}{\left(\omega_p^2(\omega)-\varepsilon_\infty\omega^2\right)^2+(\varepsilon_\infty\omega\gamma(\omega))^2} \quad \text{(H)}$$

The unscreened plasma frequency ω_p is almost energy-independent, provided that $\gamma(\omega)$ and $m^*(\omega)$ do not depend on ω too strongly. The energy-loss function is a quasi-Lorentzian function that peaks at the energy of $\omega_p^* = \omega_p/\sqrt{\varepsilon_\infty}$ which is called the screened plasma frequency. Therefore, we can identify ω_p^* by the position of the maximum of the energy-loss function, as can be seen on figure S40: we find $\omega_p^* = 1.25$ eV for the sample CVO 500 °C.

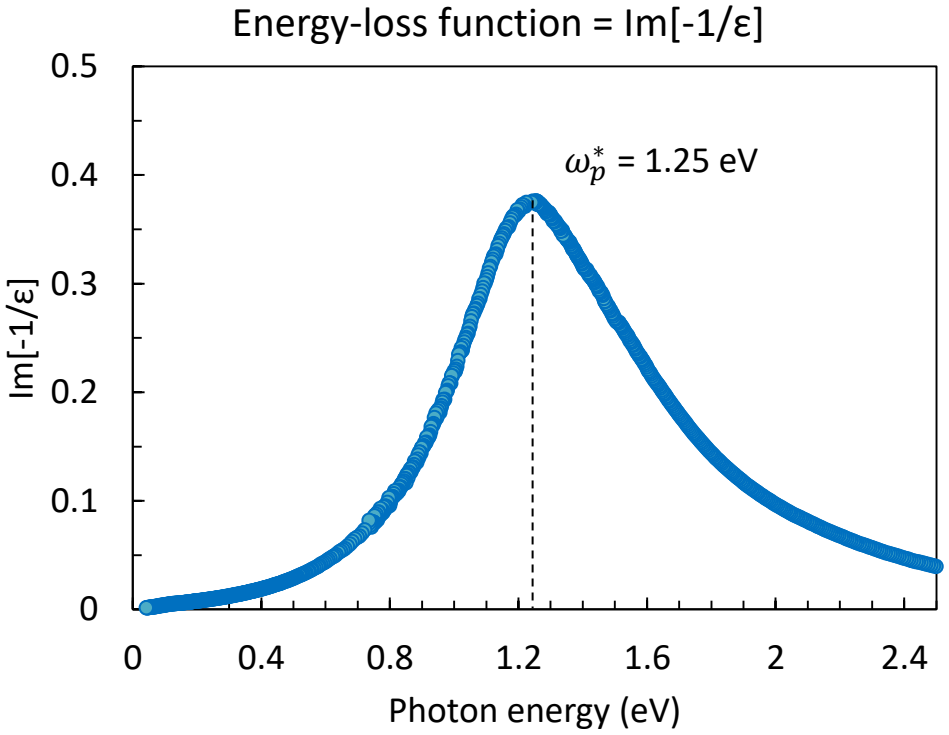

Figure S40. Energy-loss function for the crystallized CVO inside the CVO (SVO) layer of the sample CVO 500 °C with the ABEMA + Wavelength-by-wavelength fit.

4.7.2.3.Unscreened plasma frequency ω_p

To estimate the unscreened plasma frequency $\omega_p = \omega_p^* \times \sqrt{\varepsilon_\infty}$, we need to estimate the value of ε_∞. This can be done easily with the oscillator model for crystalline CVO detailed previously: we simply remove the Drude oscillator from the model and take ε_∞ as the minimum value of ε_1 in the NIR-visible range (0.7 to 2.5 eV), as shown on figure S41 for the sample CVO 500 °C. By doing so, a typical value of $\varepsilon_\infty = 5$ was estimated, and further taken as a constant for all the CVO and SVO samples. A unique value was chosen for all the samples in order to avoid adding artificial variations from sample to sample due to the specificity of the oscillators' model, which is not necessarily unique for each sample. By this method, the unscreened plasma frequency of the sample CVO 500 °C can be estimated as $\omega_p = 2.81$ eV.

The same method was applied by Makino *et al.*[13] in their study of the optical properties of $Ca_{1-x}Sr_xVO_3$ samples: they chose a constant value of $\varepsilon_\infty = 4$ for all samples by looking at the average value of ε_1 in the NIR-visible range. However, they did not remove the influence of the Drude oscillator, which has the effect of lowering significantly the ε_1 value. Therefore, we believe that a value of $\varepsilon_\infty = 5$ estimated by removing the Drude oscillator from our model is physically more meaningful.

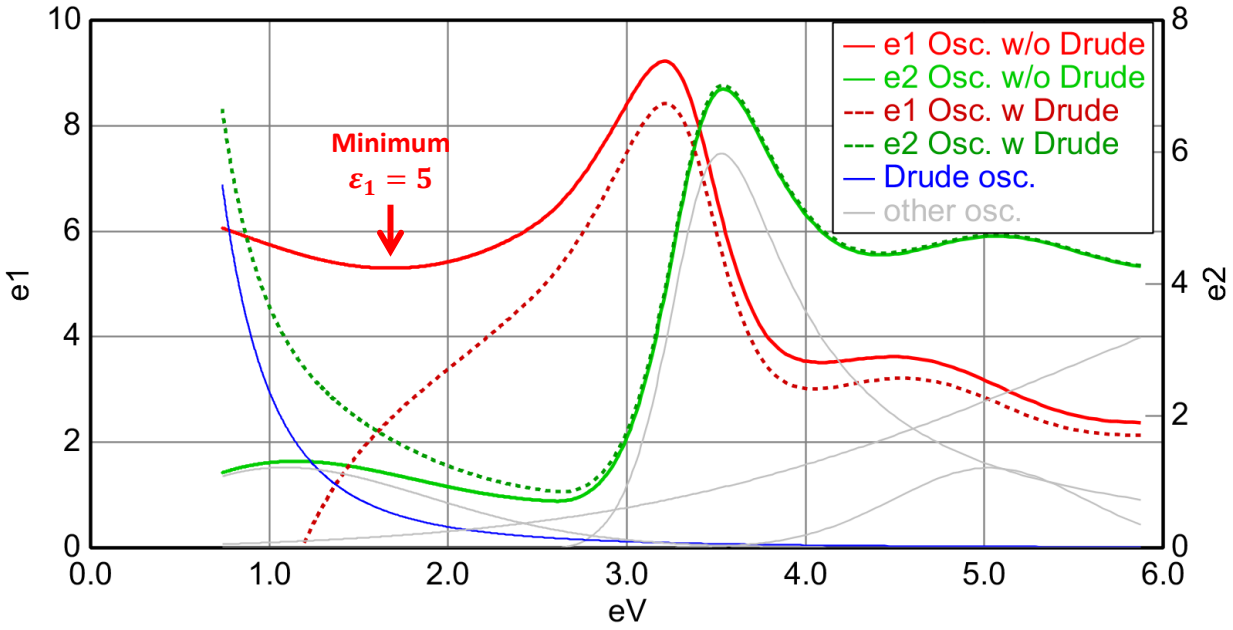

Figure S41. Dielectric functions for the crystallized CVO inside the CVO (SVO) layer of the sample CVO 500 °C with the ABEMA model (red and green), as calculated with (dashed line) or without (plain line) the Drude oscillator. The blue thin line represent the contribution of the Drude oscillator, and the grey thin lines the contributions of the others oscillators. A minimum of $\boldsymbol{\varepsilon_1 = 5}$ can be identified between 0.7 to 2.5 eV for the model without the Drude oscillator (red plain line).

4.7.2.4. Frequency-dependant scattering rate and effective mass

From the expression of the dielectric functions $\varepsilon(\omega) = \varepsilon_1(\omega) + i\varepsilon_2(\omega)$ in the generalized Drude model, one can express directly the frequency-dependant scattering rate $\gamma(\omega)$ and effective mass $m^*(\omega)$ as follows:

$$\gamma(\omega) = \frac{\omega\varepsilon_2(\omega)}{\varepsilon_\infty - \varepsilon_1(\omega)} \quad \text{(I)}$$

$$m^*(\omega) = \frac{Ne^2}{\varepsilon_0 m_e \omega^2} Re\left[\frac{1}{\varepsilon_\infty - \varepsilon(\omega)}\right] = \frac{Ne^2}{\varepsilon_0 m_e \omega^2} \frac{\varepsilon_\infty - \varepsilon_1(\omega)}{(\varepsilon_\infty - \varepsilon_1(\omega))^2 + \varepsilon_2^2(\omega)} \quad \text{(J)}$$

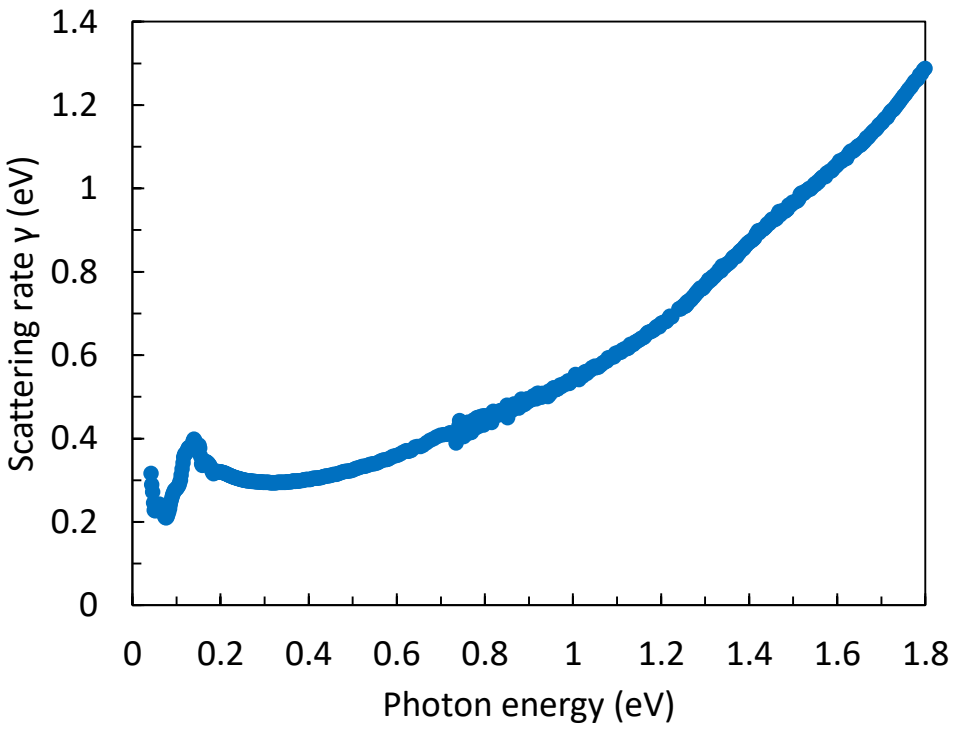

Figure S42. Energy-dependant scattering rate for the crystallized CVO inside the CVO (SVO) layer of the sample CVO 500 °C with the ABEMA + Wavelength-by-wavelength fit.

The scattering rate, as presented on figure S42, is found to have an almost linear dependence on the energy. As the temperature dependence of the resistivity shows a clear $\sim T^2$ dependence typical of a free electrons system dominated by electron-electron interaction, one would expect a $\sim \omega^2$ dependence, typical of a Fermi liquid. This linear dependence in ω is thus surprising and so far unexplained, as it was already observed by Makino *et al.*[13].

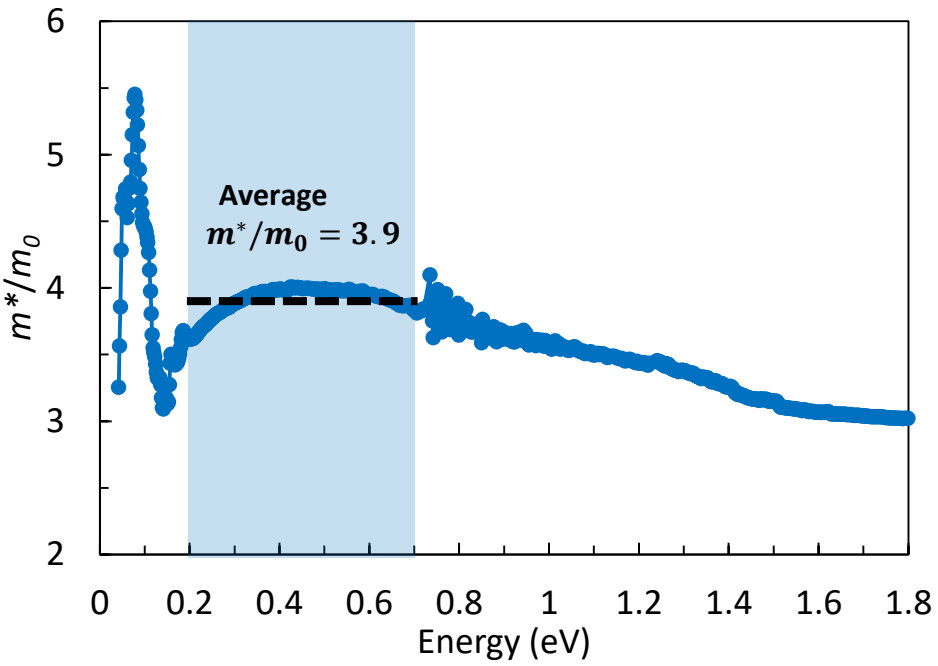

Figure S43. Energy-dependant effective mass for the crystallized CVO inside the CVO (SVO) layer of the sample CVO 500 °C with the ABEMA + Wavelength-by-wavelength fit. An average of $\boldsymbol{m^*/m_0 = 3.9}$ is found for the 0.2 to 0.7 eV spectral region.

Regarding the effective mass estimated with the carrier density $N = 2.3 \times 10^{23}$ cm^{-3} obtained from the DC Hall effect measurement, its dependency on the energy is rather weak. As shown figure S43, m^*/m_0 can be taken as a constant value of about 3.9 for CVO. This is indeed the average value in the IR spectral region from 0.2 to 0.7 eV, where the generalized Drude analysis is the most reliable, as we are far enough from the interband transitions taking place in the NIR-visible range, i.e. the free-carrier absorption dominates the dielectric properties. Below 0.2 eV on the other hand, the absorption peaks of the Eagle XG Corning® glass substrate make the analysis quite noisy. $m^*/m_0 = 3.9$ also corresponds to the value measured by Makino *et al.*[13], which indicates the good quality of our samples as well as the reliability of the analysis.

4.8. Results for all the samples: dielectric functions and effective masses

The figures S44 and S45 show the DFs and the effective masses results extended to the all of the CVO and SVO samples and determined on the basis of the SE model developed above for CVO films grown at 400 °C and 500 °C. Extracted m^*/m_0 values are summarized in table S3.

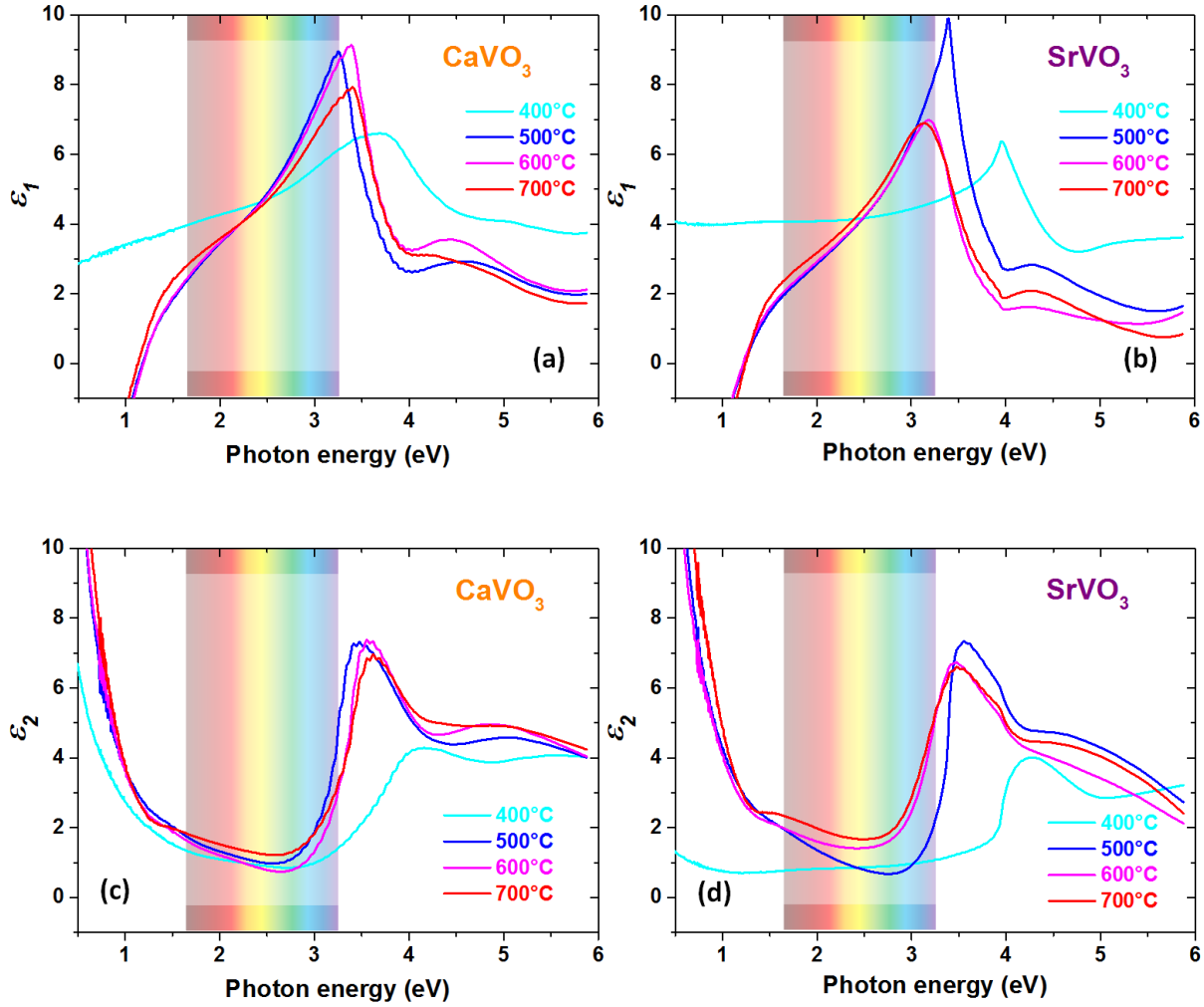

Figure S44. Real (ε_1) and imaginary parts (ε_2) of the complex permittivity $\varepsilon(\omega) = \varepsilon_1(\omega) + i\,\varepsilon_2(\omega)$ of CVO and SVO, in the IR to UV range, for the thin films deposited on CNO NS/GS. ε_1 and ε_2 are obtained by a Wavelength-by-wavelength fit and an isotropic model for the samples deposited at 400 °C (amorphous form), and by a Wavelength-by-wavelength fit with the ABEMA model for the samples deposited at 500, 600 and 700 °C (crystalline form).

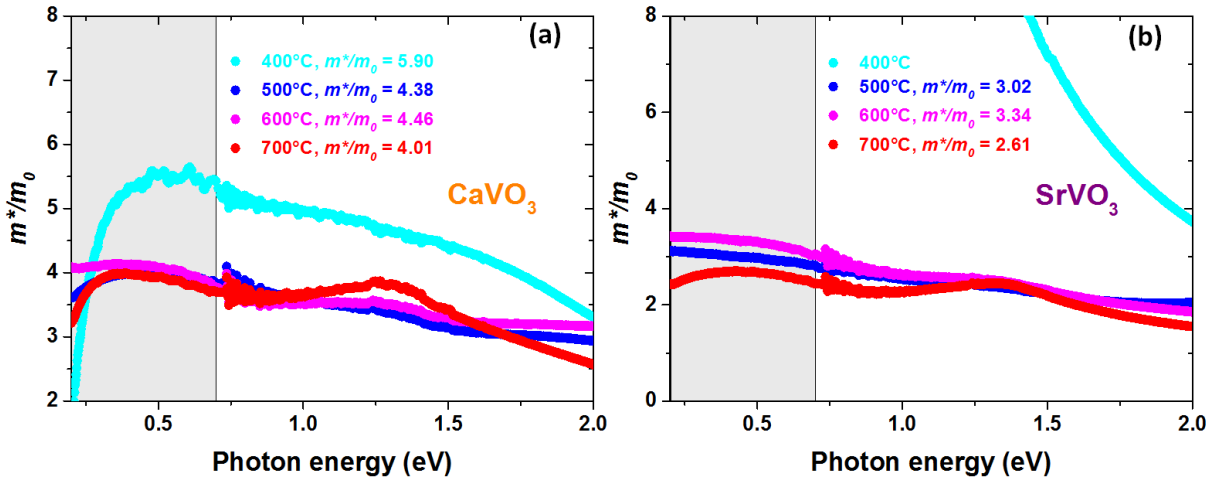

Figure S45. Energy-dependant effective mass for the crystallized CVO (a) and SVO (b) inside the CVO (SVO) films calculated from the ABEMA + Wavelength-by-wavelength fit. An average m^*/m_0 in the range of 0.2 to 0.7 eV photon energy where the generalized Drude analysis is the most reliable (grey zone).

Table S3. Summarized data of the ellipsometric measurements of CVO and SVO films on CNO NS/GS

Sample	T_G [°C]	$\rho_{opt,300K}\times10^{-4}$ [Ω.cm]	$N_{opt}\times10^{22}$ [cm^3]	μ_{opt} [cm^2.V^{-1}.s^{-1}]	τ_{opt} [fs]	m^*/m_0 [-]	ω_p [eV]	ω_p^* [eV]
CVO	400	19.88	1.48	0.21	0.46	4.70	1.88	0.84
CVO	500	2.69	2.34	0.99	7.27	3.90	2.80	1.25
CVO	600	2.60	2.27	1.06	4.46	4.08	2.78	1.24
CVO	700	4.49	2.43	0.57	1.55	3.83	2.67	1.20
SVO	400	131.92	0.03	0.07	-	-	-	-
SVO	500	2.82	1.98	1.12	4.75	3.02	2.99	1.34
SVO	600	2.74	1.71	1.33	4.61	3.34	2.90	1.30
SVO	700	3.26	2.23	0.86	1.91	2.61	2.90	1.30

Legend: Growth temperature (T_G), optical room temperature resistivity (ρ_{300K}), optical charge carrier density (N_{opt}), optical charge carrier mobility (μ_{opt}), optical scattering time (τ_{opt}), charge carrier effective mass (m^*/m_0), unscreened plasma frequency (ω_p), screened plasma frequency (ω_p^*).

5. Comparison between the DC and the optical resistivities

In this section, we shall discuss the comparison between the optical resistivity ρ_{opt} and the DC resistivity ρ_{DC}.

5.1. Connectivity of the crystalline network

Firstly, as the amorphous phase is insulating, ρ_{DC} depends on *(i)* the intrinsic DC resistivity ρ_{DC}^{cryst} of the crystalline template, *(ii)* the proportion of the crystalline phase f, and *(iii)* the quality of the geometrical connectivity between adjacent crystalline regions.

- When this connectivity is maximum, all the crystalline parts contribute equally to the transport (there are no "dead branches" nor "weak links" in the crystalline network). In this case, the crystalline and amorphous parts act as parallel resistors: if L, w, and t are the length, width and thickness of the sample, they can be seen for example as parallel stripes occupying a total width of $w \times f$ and $w \times (1-f)$ respectively, as illustrated schematically on figure S46 on the left. Thus, their resistances are respectively $R_{crystalline} = \rho_{DC}^{cryst} \frac{L}{wt \times f}$ and $R_{amorphous} = \infty$, and therefore the resistance of the sample is simply $R = \rho_{DC} \frac{L}{w} = R_{crystalline}$. As a result, the macroscopic effective resistivity is simply $\rho_{DC} = \rho_{DC}^{cryst}/f$.

- When this connectivity is minimum, there is no percolation at all: the crystalline and amorphous parts act as series resistors, as illustrated on figure S46 on the right. As a result, the macroscopic effective resistivity is simply $\rho_{DC} = \infty$.

In the general case, it is possible to link ρ_{DC} to ρ_{DC}^{cryst} by using for example an Effective Medium Approximation (EMA) in the framework of the Bruggemann model. Percolation behaviour is not correctly described by the EMA scheme, especially close to the percolation threshold, but it allows one to identify the main tendencies and provides correctly the extreme values. Considering a mixture of the crystalline phase of resistivity ρ_{DC}^{cryst} in proportion f and the insulating amorphous phase of resistivity $\rho = \infty$, the macroscopic resistivity ρ_{DC} can be expressed as[23]:

$$\rho_{DC} = \rho_{DC}^{cryst} \frac{1-L}{f-L} \qquad \text{(K)}$$

This formula is valid for $f > L$: else, there is no percolation and $\rho_{DC} = \infty$. Here L is the DC depolarization factor, which is between 0 and 1. In this EMA scheme, all the information about the long-range connectivity is included in the value of L, which is distinct from the optical depolarization factor which probes the short-range shape of the crystalline inclusions. The case of maximum connectivity (figure S46, left) corresponds to $L = 0$ (elongated stripes parallel to the DC current), for which one recovers the formula $\rho_{DC} = \rho_{DC}^{cryst}/f$ discussed above. The case of minimum connectivity (figure S46, right) corresponds to $L = 1$ (elongated stripes perpendicular to the DC current), for which one recovers $\rho_{DC} = \infty$ whatever the value of f. As an example of intermediate connectivity, the case of flat cylindrical inclusions corresponds to $L = {}^1/_2$ for which the Bruggemann formula gives $\rho_{DC} = \rho_{DC}^{cryst}/(2f - L)$ (figure S46, middle).

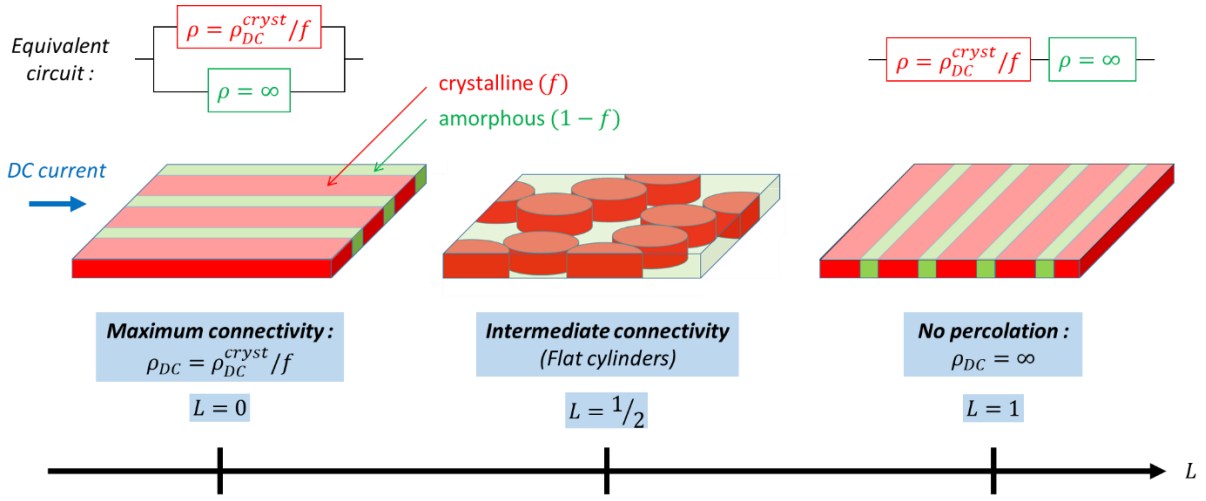

Figure S46. Scheme of the different possible configurations for the connectivity of the crystalline network and the equivalent circuits, pictured as a function of the depolarization factor L in the Bruggemann Effective Medium Approximation.

5.2. Optical vs DC resistivity

Secondly, DC measurements probe the long-range conductivity, while the optical measurements only probe the motion of the free electrons on a very short length scale (typically of a few nanometers at visible wavelengths). Therefore, ρ_{opt} corresponds to the

resistivity within a single crystalline grain, while ρ_{DC}^{cryst} also encompasses the inter-grain scattering, as well as the losses due to an imperfect geometrical connectivity between crystalline regions, so that in general $\rho_{DC}^{cryst} \geq \rho_{opt}$ (see e.g. ref.[24]).

As a result, if for a given sample we have $\rho_{DC} = \rho_{opt}$, it indicates that the grain boundary scattering is negligible ($\rho_{DC}^{cryst} = \rho_{opt}$), and also that the connectivity is maximum ($\rho_{DC} = \rho_{DC}^{cryst}/f$), as there are no increase in resistivity while going from the short-range to the long-range measurement.

6. Comparison of the transmittance efficiency of vanadate thin films with ITO and $SrNbO_3$ thin films: colorimetry of films

The spectral transmittance performance of a TCO has to be estimated over a spectral range adapted to its application. In case of photovoltaic (PV) application, the photons involved in photoconversion are absorbed over a broad spectral range, including the yellow. For this reason, we propose to estimate its spectral performance over the wide spectral range, by including the source's irradiance. In order to give a response on the CVO and SVO coloration impact on potential application, we construct the transmittance efficiency $\epsilon_{T(\lambda)}^{AM1.5\,G}$ of the reference solar spectral irradiance AM1.5 global ($Ir^{AM1.5\,G}$) by the material thin film transmittance $T(\lambda)$ as follow:

$$\epsilon_{T(\lambda)}^{AM1.5\,G} = 100.\frac{\int_{\lambda_{min}}^{\lambda_{max}} T(\lambda) Ir^{AM1.5\,G}(\lambda) d\lambda}{\int_{\lambda_{min}}^{\lambda_{max}} Ir^{AM1.5\,G}(\lambda) d\lambda} \qquad \text{(L)}$$

This transmittance efficiency is correlated to a specific spectral irradiance over a framed spectral range $[\lambda_{min}, \lambda_{max}]$. Transmittance includes intrinsic absorption effects and extrinsic effects due for example to finite thickness or to surface roughness leading respectively to interferences or scattering. Due to its broad and polychromatic nature, the Air Mass 1.5 (AM1.5) [25,26] Global irradiance spectrum ($Ir^{AM1.5\,G}(\lambda)$), designed for flat PV conversion modules, was chosen. Transmittance from CVO, SVO, ITO thin films and $SrNbO_3$ (SNO) thin film identified recently as a new performing TCO vanadate in ultraviolet range, were measured and taken from references [27,28], respectively. The TCO films thickness was chosen about 40 nm and they were considered as sufficiently smooth to have negligible scattering contributions. Despite this, thin films of equal thickness will still have contributions from intrinsic absorption and extrinsic effects mixed up due to variable optical path due to refractive index differences between materials. From those transmittance spectra and AM1.5 Global irradiance, we construct the transmittance efficiency $\epsilon_{T(\lambda)}^{AM1.5\,G}$ on the 300-997 nm spectral range (figure S50). This spectral range is more or less the range of useful photons for PV conversion Si modules and includes the human eyes visible range (0.4-0.8 µm).

The Air Mass 1.5 (AM1.5) Global irradiance spectrum ($Ir^{AM1.5\,G}(\lambda)$) is designed for flat plate modules and has an integrated power of 1000 W/m^2 (100 mW.cm^{-2}). [25,26]

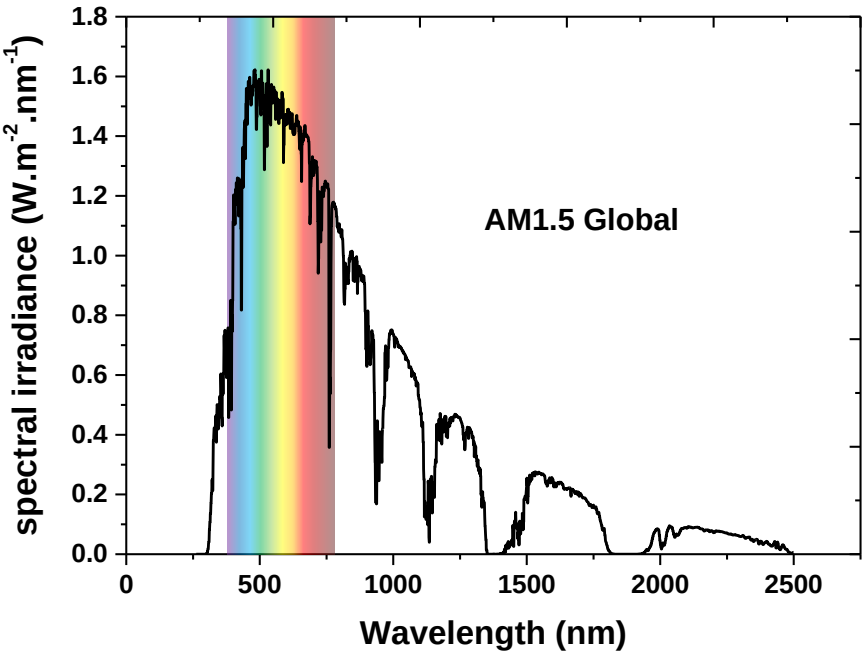

Figure S47. Air Mass 1.5 (AM1.5) Global irradiance spectrum.

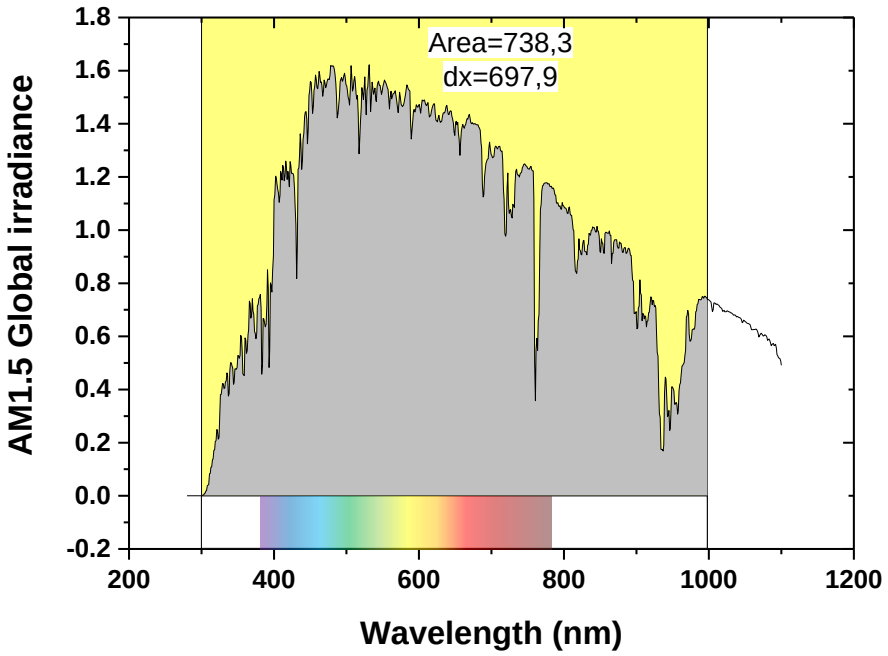

Figure S48. Air Mass 1.5 (AM1.5) Global irradiance spectrum with integration over the common spectral range 300-997 nm.

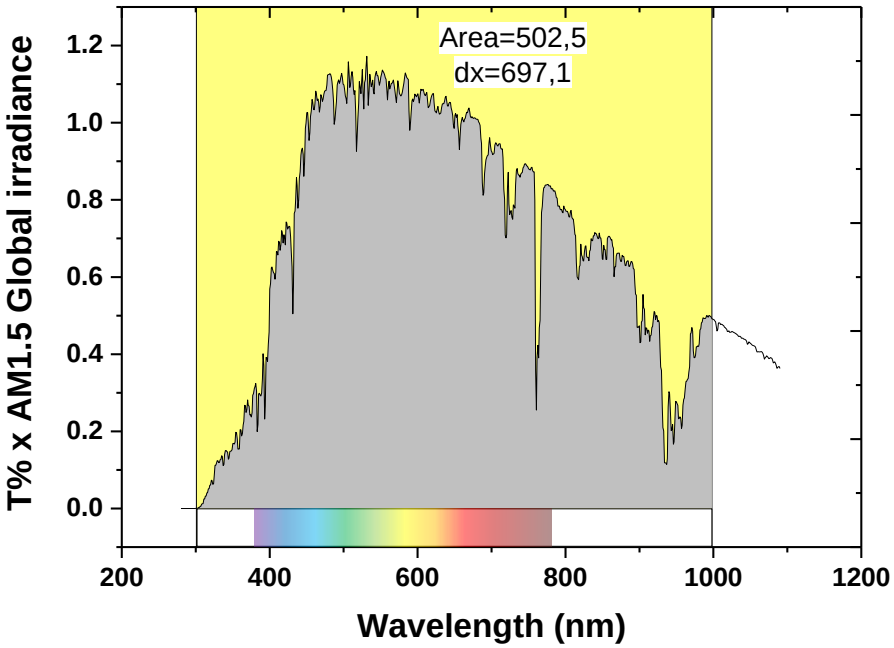

Figure S49. Function of SVO sample transmittance time the Air Mass 1.5 (AM1.5) Global irradiance spectrum with integration area over the common spectral range 300-997 nm.

The ratio of those two integrals leads to the determination of the $\epsilon_{T(\lambda)}^{AM1.5\,G}$ factor:

$$\epsilon_{T(\lambda)}^{AM1.5\ G}\ (SVO) = \frac{502.5}{738.3} \times 100 = 68.06\ \% \qquad \text{(M)}$$

For the four samples CVO, SVO, ITO, SNO we get the following results:

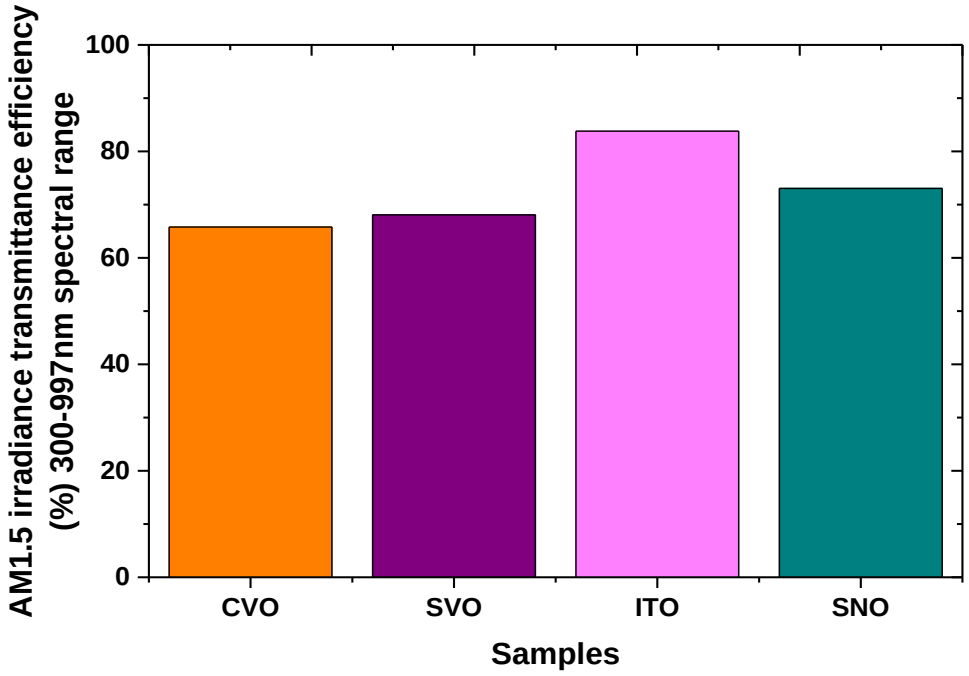

Figure S50. $\epsilon_{T(\lambda)}^{AM1.5\ G}$ for different TCO materials thin film in the 300-997 nm spectral range.

On the 300-997 nm spectral range, the ITO transmits better the AM1.5 G solar irradiance; second the SNO film followed by the SVO and the CVO. Note that the spectral range was chosen to be the largest range common to the 4 samples. The data were interpolated in order to have the same integration step of 1 nm.

References:

[1] A. Boileau, M. Dallocchio, F. Baudouin, A. David, U. Lüders, B. Mercey, A. Pautrat, V. Demange, M. Guilloux-Viry, W. Prellier, A. Fouchet, *ACS Appl. Mater. Interfaces* **2019**, *11*, 37302.

[2] F. Baudouin, V. Demange, S. Ollivier, L. Rault, A. S. Brito, A. S. Maia, F. Gouttefangeas, V. Bouquet, S. Députier, B. Bérini, A. Fouchet, M. Guilloux-Viry, *Thin Solid Films* **2020**, *693*, 137682.

[3] P. Dougier, J. C. C. Fan, J. B. Goodenough, *J. Solid State Chem.* **1975**, *14*, 247.

[4] T. Maekawa, K. Kurosaki, S. Yamanaka, *J. Alloys Compd.* **2006**, *426*, 46.

[5] Y. C. Lan, X. L. Chen, M. He, *J. Alloys Compd.* **2003**, *354*, 95.

[6] L. Zhang, Y. Zhou, L. Guo, W. Zhao, A. Barnes, H.-T. Zhang, C. Eaton, Y. Zheng, M. Brahlek, H. F. Haneef, N. J. Podraza, M. H. W. Chan, V. Gopalan, K. M. Rabe, R. Engel-Herbert, *Nat. Mater.* **2015**, *15*, 204.
[7] A. Boileau, A. Cheikh, A. Fouchet, A. David, C. Labbé, P. Marie, F. Gourbilleau, U. Lüders, *Adv. Opt. Mater.* **2019**, *7*, 1801516.
[8] A. Fouchet, M. Allain, B. Bérini, E. Popova, P.-E. Janolin, N. Guiblin, E. Chikoidze, J. Scola, D. Hrabovsky, Y. Dumont, N. Keller, *Mater. Sci. Eng. B* **2016**, *212*, 7.
[9] S. C. Dixon, D. O. Scanlon, C. J. Carmalt, I. P. Parkin, *J. Mater. Chem. C* **2016**, *4*, 6946.
[10] M. Onoda, H. Ohta, H. Nagasawa, *Solid State Commun.* **1991**, *79*, 281.
[11] V. Giannakopoulou, P. Odier, J. M. Bassat, J. P. Loup, *Solid State Commun.* **1995**, *93*, 579.
[12] M. Gu, S. A. Wolf, J. Lu, *Appl. Phys. Lett.* **2013**, *103*, 223110.
[13] H. Makino, I. H. Inoue, M. J. Rozenberg, I. Hase, Y. Aiura, S. Onari, *ArXiv Prepr. Cond-Mat9801086* **1997**.
[14] I. H. Inoue, O. Goto, H. Makino, N. E. Hussey, M. Ishikawa, *Phys. Rev. B* **1998**, *58*, 4372.
[15] J. A. Moyer, C. Eaton, R. Engel-Herbert, *Adv. Mater.* **2013**, *25*, 3578.
[16] C. Marie Nelson, M. Spies, L. S. Abdallah, S. Zollner, Y. Xu, H. Luo, *J. Vac. Sci. Technol. Vac. Surfaces Films* **2012**, *30*, 061404.
[17] X. Liang, Y. Zhang, D. Li, B. Wen, D. Jiang, M. Chen, *Appl. Surf. Sci.* **2019**, *466*, 863.
[18] P. Xu, T. J. Milstein, T. E. Mallouk, *ACS Appl. Mater. Interfaces* **2016**, *8*, 11539.
[19] K. S. Virdi, Y. Kauffmann, C. Ziegler, P. Ganter, P. Blaha, B. V. Lotsch, W. D. Kaplan, C. Scheu, *J. Phys. Chem. C* **2016**, *120*, 11170.
[20] F. Maudet, B. Lacroix, A. J. Santos, F. Paumier, M. Paraillous, S. Hurand, A. Corvisier, C. Marsal, B. Giroire, C. Dupeyrat, R. García, F. M. Morales, T. Girardeau, *Appl. Surf. Sci.* **2020**, *520*, 146312.
[21] J. W. Allen, J. C. Mikkelsen, *Phys. Rev. B* **1977**, *15*, 2952.
[22] B. C. Webb, A. J. Sievers, T. Mihalisin, *Phys. Rev. Lett.* **1986**, *57*, 1951.
[23] V. D. Bruggeman, *Ann. Phys.* **1935**, *416*, 636.
[24] J. Steinhauser, S. Faÿ, N. Oliveira, E. Vallat-Sauvain, C. Ballif, *Appl. Phys. Lett.* **2007**, *90*, 142107.
[25] C. A. Gueymard, *Sol. Energy* **2004**, *76*, 423.
[26] S. R. Kurtz, D. Myers, T. Townsend, C. Whitaker, A. Maish, R. Hulstrom, K. Emery, *Sol. Energy Mater. Sol. Cells* **2000**, *62*, 379.
[27] https://www.pgo-online.com/intl/ito.html
[28] J. Roth, A. Paul, N. Goldner, A. Pogrebnyakov, K. Agueda, T. Birol, N. Alem, R. Engel-Herbert, *ACS Appl. Mater. Interfaces* **2020**, *12*, 30520.